Fatty acid oxidation impairs macrophage effector functions that control *Mycobacterium tuberculosis*

Pallavi Chandra[1,2], Li He[3, 4], Matthew Zimmerman[5], Guozhe Yang[1,2], Stefan Köster[6,#], Mireille Ouimet[7,†], Han Wang[5], Kathyrn J. Moore[7], Véronique Dartois[5], Joel D. Schilling[3, 4], and Jennifer A. Philips[1,2*]

[1]Division of Infectious Diseases, Dept. of Medicine; [2]Dept. of Molecular Microbiology; [3]Dept. of Pathology and Immunology; [4]Cardiovascular Division, Dept. of Medicine; Washington University School of Medicine, St. Louis, MO 63110; [5] Center for Discovery and Innovation, Hackensack Meridian Health, Nutley, NJ 07003; [6]Division of Infectious Diseases and Immunology, Department of Medicine, New York University Medical Center, New York, NY, 10016, USA. [7]Marc and Ruti Bell Vascular Biology and Disease Program, Leon H. Charney Division of Cardiology, Department of Medicine, New York University Medical Center, New York, NY, 10016, USA.

[#]Current affiliation: Sanofi NA BT Lab, 270 Albany St, Cambridge, Massachusetts, 02139

[†]Current affiliation: Department of Biochemistry, Microbiology, and Immunology, University of Ottawa, Ottawa, Ontario, Canada

*Correspondence: philips.j.a@wustl.edu

SUMMARY

Macrophage activation involves metabolic reprogramming to support antimicrobial cellular functions. How these metabolic shifts influence the outcome of infection by intracellular pathogens remains incompletely understood. *M. tuberculosis* (Mtb) modulates host metabolic pathways and utilizes host nutrients, including cholesterol and fatty acids, to survive within macrophages. We found that intracellular growth of Mtb depends on host fatty acid catabolism: when host fatty acid β-oxidation (FAO) was blocked chemically with trimetazidine, a compound in clinical use, or genetically by deletion of the mitochondrial fatty acid transporter carnitine palmitoyltransferase 2 (CPT2), Mtb failed to grow in macrophages and its growth was attenuated in mice. Global metabolic profiling and mechanistic studies support a model in which inhibition of FAO generates mitochondrial reactive oxygen species, which enhance macrophage NADPH oxidase and xenophagy activity to better control Mtb infection. Thus, FAO inhibition promotes key antimicrobial functions of macrophages and overcomes immune evasion mechanisms of Mtb.

INTRODUCTION

Macrophages are at the forefront of innate immune defense and are required for microbial killing, tissue homeostasis and repair, inflammation, and development. A wealth of scientific studies describes how these cells recognize pathogen-associated molecular patterns (PAMPs), which activate downstream signaling cascades to drive pro-inflammatory responses and resolve infection. Macrophage activation involves profound metabolic reprogramming to support specific phenotypic functions. Exposure of macrophages to stimuli such as IFN-γ and LPS induces an inflammatory phenotype characterized by enhanced glycolytic metabolism and impaired oxidative phosphorylation (OXPHOS), similar to the Warburg effect described for cancer cells. Glucose

47 catabolism provides a rapid means to generate ATP, and boosts the pentose phosphate pathway
48 (PPP) and tricarboxylic acid (TCA) cycle for the generation of important immuno-metabolites
49 such as NADPH, itaconate, and prostaglandins (Galván-Peña and O'Neill, 2014; Kelly and O'Neill,
50 2015; Van den Bossche et al., 2017). On the other hand, cytokines such as IL-4 induce an anti-
51 inflammatory phenotype in macrophages important for tissue homeostasis and anti-parasitic
52 responses. These alternatively activated macrophages have increased FAO and OXPHOS (Galván-
53 Peña and O'Neill, 2014). The majority of studies on macrophage metabolism focus on IFNγ/LPS-
54 and IL-4-induced states, although accumulating evidence suggests that macrophage polarization
55 states are multi-dimensional (Xue et al., 2014). The metabolic characterization of more diverse
56 macrophage phenotypes, and their impact on antimicrobial capacity in the context of specific
57 infections is largely unexplored.
58
59 Recent studies also highlight a link between *Mycobacterium tuberculosis* (Mtb) pathogenesis and
60 host metabolism. Mtb is the causative agent of tuberculosis (TB), which kills more people yearly
61 than any other infection. Macrophages are a main cellular niche of Mtb (Cohen et al., 2018; Wolf
62 et al., 2007). Within the lung, alveolar (AM) and interstitial (IM) macrophages are the major
63 populations of infected macrophages, and they have distinct metabolic profiles. AMs, which
64 preferentially utilize FAO, represent a permissive niche for Mtb replication, whereas glycolytically
65 active IMs restrict infection (Huang et al., 2018). Mtb alters macrophage metabolism along with
66 shifting macrophage phenotype to a more pro-inflammatory state (Arts et al., 2016; Cumming et
67 al., 2018; Gleeson et al., 2016; Ouimet et al., 2016; Shi et al., 2015). Mtb enhances the dependency
68 of mitochondrial oxidative metabolism on fatty acids, in particular exogenous fatty acids, and
69 induces the formation of lipid-droplet-filled or "foamy" macrophages (Cumming et al., 2018;

Peyron et al., 2008a; Russell et al., 2009; Singh et al., 2012). Foamy macrophages are found within the inner layers of granulomas, a common histopathologic feature of TB, and the bacilli themselves can be found in close approximation to intracellular lipid droplets. It is thought that lipid bodies serve as a source of nutrients in the form of cholesterol esters and fatty acids for the bacilli, thus providing a hospitable niche for the bacterium (Brzostek et al., 2009; Daniel et al., 2011; Marrero et al., 2010; Munoz-Elias and McKinney, 2005; Pandey and Sassetti, 2008; Peyron et al., 2008b; Singh et al., 2012). Moreover, a growing body of literature suggests a link between lipid metabolism and cellular control of Mtb. A number of host-directed therapies (HDTs) under investigation for TB, such as statins and metformin, modulate host lipid metabolism (Parihar et al., 2014; Singhal et al., 2014). However, how these metabolic shifts influence the outcome of Mtb infection remains incompletely understood.

Cellular regulators of lipid metabolism such as microRNA-33 (miR-33) and the transcription factors PPAR-α and PPAR-γ play a role in the formation of Mtb-induced lipid droplets. Studies in which miR-33, PPAR-α, and PPAR-γ were modulated revealed a correlation between cellular lipids and intracellular survival of mycobacteria, such that increased intracellular lipids were associated with enhanced bacterial replication (Almeida et al., 2009; Kim et al., 2017; Ouimet et al., 2016). These studies led to the idea that impaired host fatty acid catabolism and the formation of foamy macrophages serves to enhance intracellular survival of Mtb, but direct evidence is lacking. Indeed, miR-33, PPAR-α, and PPAR-γ impact diverse aspects of host biology that influence the antimicrobial capacity of macrophages, including mitochondrial function and autophagy, and a causal link between the lipid changes they induce and the survival benefit to the bacilli has not been clearly established. Previously, we showed that induction of miR-33/33* in

response to Mtb enhances intracellular survival of Mtb (Ouimet et al., 2016). We showed that this pro-bacterial function of miR-33/33* was related in part to its ability to block autophagy, and we speculated that its ability to block fatty acid catabolism and promote the formation of lipid droplets also enhanced bacterial replication. Here, we tested whether blocking fatty acid catabolism indeed promotes Mtb replication, as prevailing models predict. Instead, we found that inhibiting macrophage FAO chemically or genetically restricted intracellular growth of Mtb. FAO inhibition promoted a pathway of bacterial killing in which induction of mitochondrial ROS (mitoROS) lead to NADPH oxidase and autophagy-dependent control of Mtb.

RESULTS

Inhibiting FAO restricts growth of intracellular Mtb

miR-33 inhibits FAO by targeting genes such as carnitine palmitoyltransferase 1 (CPT-1) and the hydroxyacyl-CoA dehydrogenase trifunctional multienzyme complex subunit beta (HADHB). CPT-1 is required for the entry of long chain fatty acids into the mitochondrial matrix, while HADHB catalyzes the final step of β-oxidation. Small molecule inhibitors, etomoxir (ETM), oxfenicine (OXF), and trimetazidine (TMZ) also target these steps in FAO. ETM and OXF inhibit CPT-1, whereas TMZ blocks the 3-ketoacyl-CoA thiolase activity of HADHB (**Figure 1A**). Thus, to determine whether the inhibition of FAO conferred by miR-33 contributed to its ability to enhance the intracellular survival of Mtb, we tested the effect of chemical inhibition of FAO on intracellular bacterial replication. We infected murine bone marrow-derived macrophages (BMDMs) with the H37Rv strain of Mtb, and four hours later, we supplemented the media with ETM, OXF, or TMZ. After treatment, we estimated intracellular Mtb growth by plating for colony forming units (CFU) at 72 hours post infection (hpi). Unexpectedly, treatment with all three FAO

inhibitors restricted the intracellular growth of Mtb compared to untreated controls. We observed a dose-dependent reduction in Mtb CFUs in macrophages treated with micromolar concentrations of ETM (**Figure 1B**), while TMZ and OXF were effective at nanomolar concentrations (**Figures 1C and D**). The antitubercular activity of TMZ was corroborated using a live-dead reporter strain of Mtb (**Figure S1A**). By comparison, metformin (MET), which has previously been shown to restrict intracellular Mtb, worked at millimolar concentrations (Singhal et al., 2014) (**Figures 1B-D**). Using calcein fluorescent dye, we found that macrophage viability was unaffected by FAO inhibitors ETM and TMZ (**Figure S1B**). In addition, the inhibitors did not have direct toxicity on Mtb in broth culture (**Figure S1C and S1D**), and they enhanced macrophage control against a distantly related mycobacterium, *Mycobacterium abscessus* (**Figure S1E**). Consistent with the ability to impair FAO, TMZ enhanced cellular lipid accumulation based upon BODIPY staining (**Figure S1F**). In addition, in keeping with impaired fatty acid oxidation, TMZ treated macrophages had reduced oxygen consumption (**Figure S1G**), similar to macrophages from mice that were genetically deficient in FAO due to deletion of carnitine palmitoytransferase 2 (*Cpt2*$^{fl/fl}$ LysM-Cre^{+}*; Cpt2* cKO) (Gonzalez-Hurtado et al., 2017).

To confirm that the anti-mycobacterial activity was indeed a result of FAO inhibition, we compared the intracellular growth of Mtb in *Cpt2* cKO macrophages to littermate controls. As shown in **Figure 1E**, Mtb was significantly impaired in *Cpt2* cKO macrophages as compared to control. Moreover, FAO inhibitors lacked activity in *Cpt2* cKO macrophages, confirming their target specificity (**Figure 1F**). To determine whether FAO inhibitors were also active against Mtb in human macrophages, we treated PMA-differentiated THP-1 cells. As we found in murine macrophages, FAO inhibitors impaired Mtb growth in THP-1 cells (**Figure 1G**). Taken together,

our findings suggest that FAO inhibition enhances the ability of macrophages to control Mtb infection. Since ETM is documented to have off-target effects (Divakaruni et al., 2018) and TMZ was effective at nanomolar concentrations, we elected it for further study.

Inhibiting FAO restricts growth of Mtb *in vivo*

Given our *in vitro* findings, we investigated whether inhibition of FAO impacts mycobacterial control in mice. We compared Mtb infection in mice with myeloid-specific knockout of *Cpt2* (*Cpt2*$^{fl/fl}$ LysM-Cre^{+}*; Cpt2* cKO) and littermate controls. We exposed mice to Mtb by aerosol and estimated lung bacterial burden after 7 days. We observed that growth of Mtb was significantly reduced in *Cpt2* cKO mice compared to controls (**Figure 2A**). To determine whether chemical inhibition of FAO had antimicrobial activity in mice, we first performed pharmacokinetic (PK) studies to establish a TMZ dosing strategy (**Figure S2A and S2B**). The half-life of TMZ in people is approximately 6 hours, but in mice the half-life by oral or IV route was less than 1 hour, so we used Alzet osmotic pumps to deliver a continuous dose over 2 weeks **(Figure S2C)**. First, we examined the ability of TMZ to reduce bacterial burden during acute infection. In the first study we infected mice with 1000-2000 Mtb CFUs and treated them with saline or TMZ for 2 weeks. We found that mice treated with 16.8 mg/kg/day TMZ experienced a 67% reduction in lung bacterial burden compared to animals in the control group (**Figure 2B**). A significant decrease in spleen CFU was also observed with 16.8 mg/kg/day TMZ treatment (**Figure 2C**). In a second study, we infected mice with 3000 CFUs, tested a higher TMZ dose range, and included PK analysis of infected animals. In this study, 16.8 mg/kg/day showed a trend towards reduced bacterial growth, which was not statistically significant, while the animals receiving 50 mg/kg/day experienced a 29% reduction in bacterial burden compared to saline controls **(Figure 2D and 2E)**.

In this group, TMZ treatment did not reduce Mtb CFU in spleen. During acute infection, the majority of Mtb bacilli are found within alveolar macrophages, suggesting that TMZ was active in this cell population. As infection progresses, additional phagocytic cells, including recruited monocytes, neutrophils, and dendritic cells become increasingly infected (Cohen et al., 2018; Wolf et al., 2007). To test whether TMZ was active in the setting of chronic infection, we began TMZ treatment 5 weeks post-infection and analyzed bacterial burden after 2 weeks of drug treatment. PK analysis was performed on infected mice 5 days after start of therapy and at end of treatment. In the setting of chronic infection, we found that TMZ treatment reduced bacterial burdens in the lungs by 35%, and in the spleen by 23% and 43%, in the 16.8 mg/kg and 50 mg/kg groups **(Figure 2F and 2G).** TMZ serum concentrations of 130 ng/ml and 370 ng/ml were achieved at the end of therapy for the 16.8 and 50 mg/kg/day groups, respectively (**Figure 2H**). TMZ is approved by the European Medicines Agency to treat angina, and the C_{max} obtained after a single 40 mg oral dose in humans is 127 ng/ml. Because there is higher serum protein binding in mice than humans (**Figure S2D**), the level achieving a similar free drug concentration in mice would be approximately 164 ng/ml. Thus, TMZ showed antimycobacterial activity at drug concentrations that are used clinically. In addition, consistent with the extremely wide therapeutic index of TMZ in preclinical toxicology studies (Harpey et al., 1988), no treatment related morbidity or mortality was observed in any of the studies. Overall, we conclude that inhibiting host fatty acid metabolism restricts mycobacterial growth *in vivo.*

FAO inhibition enhances metabolic changes in macrophages in response to Mtb infection

We turned to *in vitro* studies to assess how host fatty acid metabolism was influencing control of Mtb. Given the increasing appreciation of a link between metabolism and immunity, we globally

185 profiled metabolites to assess the effect of Mtb infection alone or when macrophage FAO was
186 inhibited. Uninfected macrophages or those that had been infected for 4h were treated for 3h or
187 24h with TMZ or solvent control before profiling **(Figure 3A)**. More than 500 metabolites were
188 detected, and in agreement with previous reports, Mtb infection caused dramatic changes in
189 macrophage metabolites (**Figure 3: Figure S3; Table S1)**; we observed evidence of increased
190 glycolytic and pentose phosphate pathway (PPP) flux **(Figure 3B)**, itaconate production (**Figure**
191 **3C**), ROS and reactive nitrogen intermediates (RNI) production **(Figure 3DE, 3E and Figure**
192 **S3A)**, phospholipid and sphingomyelin changes **(Figure S3B)**, and tryptophan metabolism
193 **(Figure S3C).** As discussed below, on its own TMZ did not significantly alter metabolic profiles
194 in uninfected macrophages, but in some cases it enhanced infection-induced changes.

195

196 We observed increases in several glycolytic intermediates **(Figure 3B)**, which suggest augmented
197 glucose catabolism in Mtb-infected macrophages. Early after infection, glucose levels declined in
198 Mtb versus control groups, while glucose-6-phosphate and hexose diphosphates (detected as
199 isobar) accumulated. After 24h of Mtb infection, the glucose levels were comparable to uninfected
200 controls, but we observed accumulation in glycolytic intermediates such as phosphoenolpyruvate.
201 The magnitude of responses induced by infection appeared to be greater in TMZ-treated groups.
202 For instance, 24 hpi glucose-6-phosphate was increased 1.52-fold increase by Mtb in drug-exposed
203 cells and 1.12-fold in the absence of TMZ. Glucose can be shunted to the pentose phosphate
204 pathway (PPP) resulting in formation of NADPH reducing power and pentose intermediates for
205 nucleotide biosynthesis. We found that metabolites specific to the PPP, 5-phosphoribosyl
206 diphosphate (PRPP) and sedoheptulose-7-phosphate, increased over time in Mtb-infected

macrophages, and again, the level of these metabolites was slightly greater upon TMZ treatment **(Figure 3B, Table S1)**.

Classically activated macrophages utilize TCA cycle intermediates for anabolic process and immune pathway signaling. They have a characteristic TCA cycle breakpoint in the conversion of isocitrate to α-ketoglutarate. This allows production of itaconate, an antimicrobial metabolite, from cis-aconitate **(Figure 3C)** (Lampropoulou et al., 2016; Michelucci et al., 2013; Nair et al., 2018). A second TCA cycle breakpoint occurs after succinate. As expected, we observed markedly increased itaconate in infected macrophages, as well as elevated succinate **(Figure 3C)**. There was no substantial difference in the infection-induced elevation in itaconate or succinate in response to TMZ treatment, suggesting these metabolites did not account for the enhanced antimicrobial effect of TMZ.

The global metabolomics data also showed evidence of increased oxidative stress in Mtb infected in macrophages relative to uninfected controls, which appeared more pronounced in TMZ-treated samples compared to untreated controls. We observed elevations in citrulline levels early after infection, reflecting the activity of iNOS, which converts arginine to citrulline and NO **(Figure 3D)**. This was accompanied by significant increases in dihydrobiopterin and biopterin **(Figure S3A)**. These compounds represent oxidized forms of tetrahydrobiopterin, a cofactor in NO synthesis. Early after infection, the antioxidants glutathione and opthalmate, a compositional derivative of glutathione, were increased by infection, suggesting enhanced glutathione synthetase activity **(Figure S3A)**. This was accompanied by increases in gamma-glutamyl amino acids, which reflect the transfer of gamma-glutamyl moiety of glutathione to acceptor amino acids. (e.g.

gamma-glutamylglutamine) **(Figure S3A)**. After 24 hpi, we observed increases in betaine, dimethylglycine, S-adenosylmethionine (SAM), S-adenosylhomocysteine (SAH) and cystathione **(Figure S3A)**. These shifts could indicate increased methionine to cysteine conversion to support glutathione synthesis. Infected cells appeared to have a more oxidized intracellular milieu after TMZ treatment, as we observed more oxidized glutathione (**Figure 3E**). Additionally, at the later time point, there were greater infection-induced shifts in SAM, SAH and cystathione levels in infected TMZ-treated cells compared to untreated controls. Combined, the alterations in the glycolytic pathway, itaconate production, and redox homeostasis suggest that macrophages adopt a more M1-like metabolic phenotype in response to Mtb infection, and TMZ-induced perturbations may enhance or prolong these changes, but do not dramatically alter the response.

FAO inhibition triggers mitochondrial ROS to promote mycobacterial control

The metabolomics data did not point to a particular metabolite or metabolic pathway to explain the antimicrobial activity of TMZ. Additionally, we measured the production of TNF-α, IL-6, CXCL2, IFN-β, CCL2, and CXCL10 in response to infection and TMZ treatment, and we did not observe a cytokine-driven antimicrobial response upon TMZ treatment (**Figure S4**). Since TMZ acts in the mitochondria, a major site of ROS production, and there was evidence of an increase in oxidative stress in TMZ-treated macrophages, we examined whether FAO inhibition promotes ROS production. We treated uninfected immortalized BMDMs (iBMDMs) with TMZ and observed an increase in ROS as early as 3 hours after treatment (**Figure 4A**). Addition of mitoTEMPO, a mitochondrial ROS (mitoROS) scavenger, abolished this ROS burst, whereas DPI, which inhibits NADPH oxidase had no effect, suggesting that the ROS was induced in the mitochondria (**Figure 4A**). Toll-like receptor activation and infection with Gram negative bacteria

have previously been shown to result in mitoROS production (Mills et al., 2016; West et al., 2011), and Mtb infection induced a small amount of mitoROS (**Figure 4B**). However, significantly more ROS was generated in Mtb-infected BMDMs after TMZ treatment (**Figure 4C**). ROS levels in Mtb-infected *Cpt2* cKO BMDMs were also significantly higher than in control macrophages (**Figure 4D**). The TMZ-induced ROS still occurred in macrophages that lacked the NADPH oxidase (*Nox2* KO), consistent with a mitochondrial source (**Figure 4C**). We confirmed that TMZ induced mitoROS by using MitoSox fluorescent dye (**Figure 4E**). Combined these results demonstrate that TMZ induces ROS from a mitochondrial source after 3 hours of treatment in both infected and uninfected macrophages.

We hypothesized that FAO inhibition resulted in mitoROS generation because of perturbed electron flow within the electron transport chain (ETC). ROS can be generated in multiple sites along the ETC during forward electron transport, as well as when electrons flow in reverse through complex I (NADH:coenzymeQ reductase) (Scialò et al., 2017). To determine the site within the ETC where TMZ induced ROS, we measured mitoROS production in macrophages treated with TMZ in combination with rotenone, an inhibitor of complex I. When electrons are flowing in the forward direction, rotenone prevents electron transport to CoQ, resulting in ROS generation. In contrast during reverse electron transport (RET), rotenone reduces ROS by preventing CoQ from transferring electrons back to complex I, where the RET-ROS is generated. We treated uninfected BMDMs with TMZ for 3h, and thirty minutes prior to measuring mitoROS we added rotenone. As expected, rotenone and TMZ on their own increased mitoROS production. In contrast, rotenone decreased the amount of ROS generated in response to TMZ treatment (**Figure 4E**) These findings

275 are consistent with the idea that under conditions of TMZ treatment there is enhanced ROS
276 generated due to RET at complex I.

277

278 Since recent studies have shown that mitoROS contributes to microbial control in macrophages
279 (Abuaita et al., 2018; West et al., 2011), we asked whether TMZ-induced mitoROS was important
280 for infection control or simply a by-product of metabolic perturbations. To address this, we
281 estimated Mtb burden in macrophages treated with TMZ alone or in combination with
282 mitoTEMPO. As shown in **Figure 4F**, mitoTEMPO on its own had little effect on the infection,
283 but it partially reversed the antimicrobial effect of TMZ treatment. Overall, we conclude that FAO
284 inhibition promotes mitoROS production from the ETC, which enhances macrophage control of
285 Mtb infection.

286

287 **FAO inhibition-induced mitochondrial ROS drives NADPH oxidase recruitment to**
288 **phagosomes**

289 Previous studies suggest a link between mitoROS and NADPH oxidase that contributes to
290 macrophage defense (Garaude et al., 2016). Indeed, while 3 h of TMZ treatment significantly
291 increased mitoROS in both wt and *Nox2* KO BMDMs (**Figure 4C**), we observed that the anti-Mtb
292 activity of FAO inhibitors required NADPH oxidase (**Figure 5A**). This suggested that the
293 antimycobacterial activity in FAO-inhibited macrophages actually depended upon both a
294 mitochondrial source and NADPH oxidase. Normally, pathogen associated molecular patterns
295 (PAMPs) promote the recruitment of the NADPH oxidase to microbial phagosomes immediately
296 after phagocytosis (Nunes et al., 2013). However, Mtb impairs the recruitment of the NADPH

297 oxidase to the mycobacterial phagosome (Köster et al., 2017; Sun et al., 2013). Remarkably, at 24
298 hpi we observed that TMZ increased the recruitment of NADPH oxidase subunits gp91^{phox}/NOX2
299 and p40^{phox} to the mycobacterial phagosomes (**Figure 5B, C and D**). Moreover, we found that
300 NADPH oxidase recruitment was dependent on TMZ-induced mitoROS, as it was reversed with
301 the addition of mitoTEMPO (**Figure 5E**). Thus, FAO inhibition appears to enhance two
302 antimicrobial responses that are suboptimal during Mtb infection, mitoROS production and
303 phagosomal recruitment of the NADPH oxidase. Mitochondria alone contributed to ROS within
304 3h of FAO inhibition, while the role of NADPH oxidase was appreciable at later time points, and
305 macrophage control of Mtb depended upon both mitoROS and the NADPH oxidase.

306

307 **FAO inhibition promotes xenophagy to restrict intracellular Mtb growth**

308 TMZ treatment in Mtb-infected macrophages resulted in increases in phospholipids and
309 sphingomyelin, which might alter phagosomal trafficking (**Figure S3B**). In addition, ROS
310 generated by the NADPH oxidase promote a trafficking pathway called LC3-associated
311 phagocytosis (LAP). Both LAP and autophagy of microbes (xenophagy) are characterized by the
312 association of lipidated LC3 (LC3-II) with microbe-containing vacuoles (Martinez et al., 2015).
313 LAP and xenophagy depend upon certain common ATG (autophagy related) proteins, and they
314 also have unique requirements. To determine whether either LC3-trafficking pathway was
315 involved in the antimicrobial activity of TMZ, we compared the efficacy of TMZ between control
316 and *Atg5* cKO macrophages, which are deficient in both LAP and xenophagy. Indeed, the
317 antimycobacterial control established by FAO inhibition was reversed in *Atg5*-deficient
318 macrophages **(Figure 6A)**. Although the baseline ROS staining was lower in *Atg5* cKO
319 macrophages compared to control, ROS was still induced by TMZ in *Atg5* cKOs, suggesting that

ATG5 acts downstream of mitoROS production **(Figure 6B)**. To distinguish xenophagy from LAP, we examined *Atg14l* cKO and *Parkin2* KO macrophages, which are specifically involved in xenophagy. As we had seen in *Atg5* cKO macrophages, the antimycobacterial control established by FAO inhibition was reversed in *Atg14l* cKO and *Parkin2* KO as well (**Figure 6C and 6D**). In addition, in wt macrophages, TMZ treatment resulted in enhanced co-localization between Mtb and the autophagy adaptor, p62 (**Figure 6E**). The enhanced colocalization between Mtb and p62 occurred after 24 hours treatment and was dependent on mitoROS (**Figure 6F and 6G**). Combined, these data demonstrate that inhibition of FAO promotes xenophagy to control intracellular Mtb growth. Indeed, autophagosomal targeting of Mtb was also inherently higher in *Cpt2* cKO macrophages as compared to wt controls (**Figure 6H and 6I**). Moreover, TMZ treatment facilitated xenophagy of a mutant Mtb strain lacking *esxA* (Δ*esxA*), which is unable to perforate phagosomes and usually does not activate xenophagy (**Figure 6J**).

These studies established that FAO inhibition induced mitoROS, which promoted NADPH oxidase recruitment to the Mtb phagosome and xenophagy. Next we examined the relationship between the NADPH oxidase and xenophagy. We observed that the enhanced NADPH oxidase recruitment in response to TMZ occurred independently of autophagy, as it was also seen in *Atg5* cKO macrophages (**Figure 6K**). On the other hand, TMZ failed to promote xenophagy in NADPH oxidase-deficient macrophages (**Figure 6L**). Taken together, our data shows that mitoROS was the primary signal induced by FAO inhibition that resulted in enhanced NADPH oxidase and xenophagy, which promoted bacterial control.

DISCUSSION

Recent work has highlighted the relationship between macrophage metabolism and inflammatory phenotype (Escoll and Buchrieser, 2019). Within the context of Mtb infection, macrophages undergo a Warburg-like shift with enhanced aerobic glycolysis (Gleeson et al., 2016; Lachmandas et al., 2016; Shi et al., 2015) and usage of TCA cycle intermediates for the generation of immuno-metabolites (Nair et al., 2018). Mtb-induced glycolysis reduces intracellular bacterial survival through enhanced IL-1β production, but the impact of fatty acid metabolism is not well established. Mtb also dramatically alter host lipid metabolism, promoting the formation of lipid-droplets (Cumming et al., 2018; Peyron et al., 2008a; Russell et al., 2009; Singh et al., 2012) and increasing mitochondrial dependency on exogenous fatty acids (Cumming et al., 2018). Because Mtb can utilize host fatty acids as a carbon source during infection, a prevailing idea is that host and pathogen are in competition for resources, so that reduced host consumption or enhanced production of cellular lipids would provide a nutrient source for bacterial replication (Almeida et al., 2009; Kim et al., 2017; Ouimet et al., 2016). Instead, we found that inhibition of host FAO impaired mycobacterial replication. Our initial *in vitro* results are in concordance with a recent report that showed the efficacy of FAO inhibitor ETM in Mtb-infected BMDMs (Huang et al., 2018). In that study, the antimicrobial effect was attributed to reduced IFN-β, but ETM was used at 200 μM, which has well-documented off-target effects (Divakaruni et al., 2018). We did not see effects on Type I IFN (Figure S4), and we establish the antimicrobial mechanism of FAO inhibition using specific inhibitors and genetically FAO-deficient *Cpt2* knockout macrophages. Unexpectedly, we found that blocking FAO enhanced macrophage effector functions by eliciting mitoROS, which promoted NADPH oxidase and xenophagy to restrict Mtb infection. Our results suggest mitoROS as a connecting link between macrophage fatty acid metabolism and macrophage effector functions to control Mtb infection.

366

367 The earliest cellular response that we could detect after FAO inhibition was induction of mitoROS,
368 which occurred within three hours of treatment in both infected and uninfected macrophages.
369 Typically, FAO products, such as NADH and $FADH_2$, are oxidized by respiratory chain
370 supercomplexes to generate the forward electron flow (FET) required for ATP production. The
371 respiratory chain is organized into interacting supercomplexes to minimize leakage of electrons
372 and ROS formation. Recent studies report that enzymes of FAO also physically interact with ETC
373 components, forming an integrated, multifunctional complex (Wang et al., 2019). The FAO
374 trifunctional protein (TFP), a tetramer that includes the target of TMZ (3-ketoacyl-CoA
375 thiolase/HADHB), interacts with the NADH-binding domain of complex I. The presence of ETC
376 supercomplexes dedicated to FAO may explain why FAO inhibition leads to mitoROS. In the
377 absence of NADH shuttling from FAO to these dedicated supercomplexes, RET might occur. This
378 fits with our finding that combined treatment with TMZ and rotenone, a complex I inhibitor,
379 decreased mitoROS levels, consistent with RET generating the ROS at complex I. mitoROS is
380 also generated in response to microbial products; toll-like receptor signaling alters supercomplex
381 assembly and generates RET-ROS at complex I, both of which impact immunological signaling
382 (Garaude et al., 2016; Langston et al., 2019; Mills et al., 2016; West et al., 2011). Thus, the
383 mitoROS induced by TMZ may activate an antimicrobial pathway that is normally induced and
384 protective in the context of other infection, but suboptimal in during Mtb infection. Interestingly,
385 in distinction to our finding that FAO inhibition generated mROS, the reverse relationship was
386 seen in *Salmonella* infected zebrafish larvae and J774.2 murine macrophage cells, where FAO
387 enhanced *Salmonella*-induced mROS (Hall et al., 2013). The difference between this previous

388 study and ours could be due to the experimental systems, and it may reflect a different metabolic
389 response of macrophages to mycobacteria as compared to *Salmonella*.

390

391 The idea that FAO inhibition enhances macrophage control of Mtb by generating mitoROS is
392 consistent with recent studies showing that mitoROS contributes to macrophage control of
393 *Streptococcus pneumonia*, *Staphylococcus aureus*, and *Salmonella typhimurium* (Abuaita et al.,
394 2018; Bewley et al., 2017; Hall et al., 2013; West et al., 2011). Our results suggest that mitoROS
395 does not exert its antimicrobial function by directly killing Mtb, since mitoROS was generated in
396 macrophages lacking *Nox2* and *Atg5,* but the antimycobacterial activity was lost. Rather, mitoROS
397 appears to serve as a signal that enhances NADPH oxidase activity and xenophagy. A stimulatory
398 effect of mitoROS on the NADPH oxidase has been documented most extensively in non-
399 lymphoid cells, and recent work shows that in neutrophils mitoROS activates the NADPH oxidase
400 and other effector functions (Nazarewicz et al., 2013; Pinegin et al., 2018; Vorobjeva et al., 2017).
401 In addition to promoting the phagosomal recruitment of NADPH oxidase to mycobacterial
402 phagosomes, our metabolomics data indicate that FAO inhibition may augment the PPP, which
403 would enhance NADPH production to power the NADPH oxidase.

404

405 It will be important to understand how mitoROS promotes phagosomal assembly of the NADPH
406 oxidase. NADPH oxidase assembly requires membrane trafficking of two integral membrane
407 subunits ($p22^{phox}$ and $gp91^{phox}$) followed by recruitment of the cytosolic subunits ($p40^{phox}$, $p47^{phox}$,
408 $p67^{phox}$). Normally this occurs shortly after uptake of phagocytic cargo that activate pathogen
409 recognition receptors. In our experimental system, the kinetics are very different than what is
410 typically described. We added TMZ 4h after Mtb had been added to macrophages and when

411 extracellular bacilli had been washed away. We found that TMZ enhanced localization of both the
412 gp91^{phox} and p40^{phox} subunits with mycobacterial phagosomes 24 hours later. This suggests that
413 signals generated by mitoROS either overcome a Mtb-induced blockade to NADPH oxidase
414 recruitment or promote recruitment through a previously unappreciated pathway. How mitoROS
415 regulates phagosomal NADPH oxidase recruitment and assembly will be important to establish in
416 future studies, as our work indicates that it can be augmented, even after bacterial uptake, to
417 promote microbial clearance of intracellular bacilli. This might be a way to clear foci of persistent
418 bacilli.

419

420 In addition to NADPH oxidase recruitment, mitoROS also promoted xenophagy. Xenophagy and
421 LAP are related LC3-trafficking pathways that can promote microbial clearance (Upadhyay and
422 Philips, 2019). They also differ, as LAP occurs immediately after phagocytosis and involves LC3
423 recruitment to a single phagosomal membrane, whereas xenophagy depends upon formation of a
424 double membrane compartment. We found that the antimicrobial activity of TMZ depended on
425 ATG14L and PARKIN, which are required for canonical autophagy and Mtb xenophagy
426 (Manzanillo et al., 2013). In addition, TMZ enhanced the association of phagosomes with p62, a
427 selective autophagy adaptor, and the response occurred well after bacterial uptake, all of which
428 suggest that the mechanism of clearance is xenophagy and not LAP, despite the involvement of
429 NADPH oxidase which has been linked to LAP. We also cannot rule out that both LAP and
430 xenophagy are enhanced by FAO inhibition. In terms of how the NADPH oxidase might activate
431 xenophagy, one possibility is that the NADPH oxidase generates phagosomal membrane damage,
432 which is known to promote pathogen ubiquitination, adaptor recruitment, and xenophagy
433 (Manzanillo et al., 2012; Wong and Jacobs, 2011). We observed NADPH oxidase recruitment in

434 TMZ-treated *Atg5* cKO macrophages, yet, TMZ failed to kill Mtb in the absence of xenophagy,
435 arguing against direct antimycobacterial activity of the NADPH oxidase. The lack of direct activity
436 is consistent with other recent studies (Köster et al., 2017; Olive et al., 2018), and likely reflects
437 that Mtb has ROS-detoxifying activities such as KatG, a catalase/peroxidase. We conclude that the
438 antimycobacterial activity of ROS is primarily based upon its ability to activate lysosomal
439 trafficking pathways, perhaps due to damage to the phagosomal membrane resulting in xenophagy
440 activation.

441

442 While, the current view is that ROS generation contributes to inflammation and cellular damage,
443 a beneficial role of RET-ROS was appreciated recently for hypoxia sensing in the carotid body
444 (Fernández-Agüera et al., 2015), ischemia-reperfusion injury (Chouchani et al., 2014), and
445 extending fly lifespan (Scialò et al., 2016). A number of studies propose the use of FAO inhibitors
446 as metabolic therapy in cancer (Duman et al., 2019; Wang et al., 2018) and heart failure (Lionetti
447 et al., 2011). Given the link that we have shown between FAO inhibition and mitoROS, it will be
448 important to establish whether that contributes to their therapeutic effects. TMZ, which has been
449 used to treat angina for 35 years, is orally bioavailable, lacks substantial drug-drug interactions,
450 and has a favorable safety profile (Dézsi, 2016). Importantly, TMZ showed antimycobacterial
451 activity in mice at drug concentrations that are used clinically. Therefore, TMZ could be rapidly
452 translated into an HDT to be used as an adjunct to conventional antibiotics. The magnitude of Mtb
453 control was modest, but similar to other HDTs that have been tested in mouse models of Mtb
454 (Napier et al., 2011; Parihar et al., 2014; Singhal et al., 2014). In the case of TMZ, the limited
455 activity is probably not due to inadequate drug exposure, but may reflect that TMZ works in only
456 certain myeloid cells *in vivo,* perhaps based upon their metabolic phenotype, or that there is limited

457 capacity of mitoROS or autophagy to activate robust clearance. Distinguishing these possibilities
458 will be important in terms of designing effective HDTs for clinical use. Evaluating the effect of
459 TMZ on other cell types critical for Mtb infection, including neutrophils, dendritic cells, and T
460 cells will be important. Many of the leading candidates for HDT, such as metformin and sirtuin-1,
461 also promote autophagy (Cheng et al., 2017; Singhal et al., 2014), and whether enhanced
462 antimicrobial control could be established by a combination of HDTs that target distinct cellular
463 reservoirs or work synergistically to activate antimicrobial pathways will be critical to investigate.

464

465 **ACKNOWLEDGEMENTS**

466 We thank members of the Philips laboratory and Robert Mahon (NIH/NIAID) for critical reading
467 of the manuscript. We thank Ronald E. Dolle (Washington University in St. Louis (WUSTL)) for
468 help designing PK studies, Michael J. Wolfgang (Johns Hopkins University School of Medicine)
469 for providing Cpt2$^{fl/fl}$ mice, and Jeff Cox (University of California, Berkeley) for providing Rv-lux
470 strain. We thank the Alvin J. Siteman Cancer Center (WUSTL), Barnes-Jewish Hospital in St
471 Louis, MO, the Bursky Center for Human Immunology and Immunotherapy Programs
472 Immunomonitoring Laboratory, and Diane Bender for the multiplexing immunoassay service. The
473 Siteman Cancer Center is supported in part by an NCI Cancer Center Support Grant #P30
474 CA091842. This work was supported by grants from the NIH (R21 AI128427), the Center for
475 Drug Discovery (WUSTL), and LEAP Inventor Challenge Award (WUSTL) to J.A.P, NIH (R35
476 HL135799) to K.J.M., NIH (R01 DK11003404) to J.D.S., and the Pott's Memorial Foundation to
477 P.C.

478

AUTHOR CONTRIBUTIONS

M.O. and S.K. did experiments demonstrating activity of etomoxir against intracellular Mtb and P.C. performed all subsequent experiments. She had help with mice and MIC measurements from G. Y. and SeaHorse experiments by L.H. M.Z., H.W., and V.D. measured TMZ concentrations from serum of infected mice. J.A.P. conceived the project and supervised the experiments with input from J.D.S. P.C. and J.A.P. wrote the manuscript; P.C., S.K., M.O., K.J.M., V.D., J.D.S, and J.A.P. edited the manuscript.

DECLARATION OF INTERESTS

The authors declare no competing interests.

STAR Methods

KEY RESOURCES TABLE

REAGENT or RESOURCE	SOURCE	IDENTIFIER
Antibodies		
gp91 phox antibody	Abcam	Cat# ab80508
p40-phox (N-20-R) antibody	Santa Cruz Biotechnology	Cat# sc-18252-R
Human/Mouse/Rat p62/SQSTM1 Alexa Fluor 488 conjugated antibody	R&D systems	Cat# IC8028G
Alexa Fluor 488 goat and rabbit IgG(H+L)	Thermo Fisher Scientific	Cat#A11034
Chemicals and Inhibitors		
Etomoxir	Tocris Bioscience	Cat# 4539
Trimetazidine	Cayman Chemical Company	Cat# 18165
Oxfenicine	Sigma Aldrich	Cat# 56160-10G
Metformin	Sigma Aldrich	Cat# D150959-5G
mitoTEMPO	Sigma Aldrich	Cat# SML0737-5MG
Amikacin	Sigma Aldrich	Cat# A1774
BODIPY 493/503	Thermo Fisher Scientific	Cat# D3922
Calcein AM cell permeant dye	Thermo Fisher Scientific	Cat# C1430
Diphenyleneiodonium chloride (DPI)	Sigma Aldrich	Cat# D2926-10MG
Tert-Butyl hydroperoxide (tBHP)	Sigma Aldrich	Cat# 416665-100ML
N-acetyl L-cysteine (NAC)	Sigma Aldrich	Cat# A7250-5G
Rotenone	Sigma Aldrich	Cat#R8875
Antimycin	Sigma Aldrich	Cat#A8674
Menadione	Sigma Aldrich	Cat# M5625
Oligomycin	Sigma Aldrich	Cat#C2920
FCCP	Sigma Aldrich	Cat# P8139
Phorbol 12-myristate 13-acetate (PMA)	Sigma Aldrich	Cat# P8139
CellRox Green Reagent	Thermo Fisher Scientific	Cat# C10444
MitoSox Red mitochondrial superoxide indicator	Thermo Fisher Scientific	Cat# M36008
Deposited Data		
N/A		
Commercial Assays		
Milliplex MAP Mouse Cytokine/Chemokine Magnetic Bead Panel	EMD-Millipore	Cat# MCYTOMAG-70K
IFN-alpha/IFN-beta 2-plex Mouse ProcartaPlex Panel	Thermo Fisher Scientific	Cat# EPX02A-22187-901
Software and Algorithms		
GraphPad Prism		www.graphpad.com

NIS Elements version 4.40	Nikon, Inc	
Culture supplies and supplements		
Dulbecco's Modified Eagle Medium (DMEM)	Thermo Fisher Scientific	Cat# 11995065
RPMI 1640 Medium	Thermo Fisher Scientific	Cat# 11875093
Fetal bovine serum (FBS)	Thermo Fisher Scientific	Cat# 26140079
BD Difco Middlebrook 7H9 Broth	BD Biosciences	Cat# 271310
BD BBL Middlebrook ADC Enrichment	BD Biosciences	Cat# 212352
BD Difco Middlebrook 7H11 Agar	BD Biosciences	Cat# 283810
BD BBL Middlebrook OADC Enrichment	BD Biosciences	Cat# 212351

LEAD CONTACT AND MATERIALS AVAILABILITY

Further information and requests for reagents may be directed to and will be fulfilled by the Lead Contact, J. A. Philips (philips.j.a@wustl.edu)

EXPERIMENTAL MODEL DETAILS

Bacterial Strains

M. tuberculosis and *M. abscessus* were grown at 37°C to log phase in Middlebrook 7H9 broth (BD Biosciences) supplemented with 0.05% Tween 80, BD BBL Middlebrook ADC Enrichment (BD Biosciences), and 0.2% (vol/vol) glycerol. Plasmids were selected with 25 µg/ml kanamycin or 50 µg/ml hygromycin depending on the resistance marker. H37Rv, the wild type Mtb strain, and Δ*esxA* were provided by William Jacobs Jr. (Albert Einstein College of Medicine)(Wong and Jacobs, 2011). DsRed expressing H37Rv was a gift from J. Ernst (New York University). H37Rv expressing the *Vibrio harvei* luciferase (Rv-lux) was gift from Jeff Cox (University of California, Berkeley). The "live-dead" reporter strain constitutively expresses mCherry and inducibly express GFP under control of a tetracycline-inducible promoter (Martin et al., 2012).

518 **Mice**

519 We used 8-12 week old C57BL/6 mice. *Cpt2*$^{fl/fl}$ LysM-Cre^{+} mice were generated by crossing
520 *Cpt2*$^{fl/fl}$ and LysM-Cre^{+} mice. The generation of *Cpt2*$^{fl/fl}$ and LysM-Cre^{+} mice have been described
521 previously (Clausen et al., 1999; Lee et al., 2015). The Washington University School of Medicine
522 Institutional Animal Care and Use Committee approved all the work with mice. Euthanasia was
523 performed prior to bone marrow harvest in accordance with the 2013 *AVMA Guidelines for the*
524 *Euthansia of Animals* (https://www.avma.org/KB/Policies/Documents/euthanasia.pdf).

525

526 **METHOD DETAILS**

527 **Cell culture**

528 To obtain murine bone marrow-derived macrophages (BMDMs), marrow was flushed from the
529 femurs and tibia of mice, and the hematopoetic stem cells were allowed to differentiate for 7 days
530 in Dulbecco's Modified Eagle Medium (DMEM, Gibco) supplemented with 10% fetal bovine
531 serum (FBS, Gibco), 1% Pen-Strep solution (Gibco), and 20% L929-conditioned medium. After
532 7 days, the BMDMs were harvested using Ca^{2+}/Mg^{2+}-free PBS (Gibco) containing 5mM EDTA
533 (Invitrogen, Life Technologies), and maintained in DMEM containing 10% FBS and 10% L929-
534 conditioned medium after infection. Immortalized BMDMs (iBMDMs) were immortalized by
535 infection with the J2 retrovirus (BEI Resources). RAW 264.7 and THP-1 cells were obtained from
536 American Type Tissue Collection (ATCC) and were maintained in DMEM and RPMI-1640,
537 respectively, with 10%FBS. THP-1 differentiation was induced using 20 ng/ml phorbol-12-
538 myristate acetate (PMA, Sigma) for 18-20 hours.

539

Bacterial infections

For *in vitro* macrophage assays, a log phase culture of Mtb H37Rv was pelleted and resuspended in macrophage culture medium. Bacterial single-cell suspensions were prepared by filtering through 5-micron filters (PALL Life Sciences, catalog no. 4650). The number of Mtb in the resultant filtrate was estimated by measuring absorbance at 600 nm, followed by infection of macrophages at a multiplicity of infection (MOI) of 5. After 4 hours, macrophages were washed three times with warm DMEM to remove extracellular bacteria, and then resuspended in medium containing FAO inhibitors or solvent control. To estimate intracellular Mtb growth, infected macrophages were lysed in 0.06% SDS solution at the indicated time points, and serial dilutions of the lysates were plated on 7H11 agar plates (BD Biosciences, catalog no. 283810) containing BD BBL Middlebrook OADC Enrichment (BD Biosciences, catalog no. 212351) and glycerol. Colony forming units (CFU) were calculated 14-21 days later. For *in vivo* infections, log phase H37Rv culture was pelleted and resuspended in sterile 0.5% Tween 80 solution. After a centrifugation step, the supernatant was used for aerosol infection using a Glas-Col inhalation exposure system. The infectious dose administered was calculated by plating CFU from an aliquot of the bacterial suspension.

Mice surgeries and aerosol infections

Alzet mini-osmotic pumps (Model 2002, Durect Corporation, CA) were loaded with saline or TMZ solution as per the manufacturer's protocol. The osmotic pumps were surgically implanted in anesthetized mice under aseptic conditions. The mice were administered analgesic to minimize pain and were monitored regularly for signs of pain and other postoperative complications. Two days later, the mice were infected with H37Rv via aerosol route using an inhalation exposure

563 system from Glas-Col. The dose of infection was confirmed one day post-infection by plating
564 whole lung homogenates from 2 mice on Middlebrook 7H11 agar. 2 weeks post infection, the mice
565 were euthanized and the lungs were harvested, homogenized, and plated for CFUs.

566

567 **Serum microsampling of TMZ**

568 Serum concentrations of TMZ in mice were determined at 5 and 14 days after initiating treatment.
569 Lidocaine was applied to mice tails to minimize pain, and the end of the tail was wiped with alcohol
570 and a small incision was made. 100 µl blood was collected in K_2-EDTA microvette tubes
571 (Braintree Scientific, Inc) and was centrifuged at 5,000 rpm for 5 minutes to recover plasma.
572 Samples were stored at – 80°C until analyzed for TMZ content.

573

574 **High pressure liquid chromatography coupled to tandem mass spectrometry (LC/MS-MS)**
575 **analytical method**

576 1 mg/mL DMSO stocks of Trimetazidine (Sigma-Aldrich) were serial diluted in 50/50 Acetonitrile
577 water and subsequently serial diluted in drug free CD1 mouse plasma (K_2EDTA, Bioreclamation
578 IVT, NY) to create standard curves and quality control (QC) spiking solutions. Standards, QC,
579 controls, and study samples were extracted by combining 10 µL plasma with 100 µL
580 acetonitrile/methanol 50/50 containing the internal standard verapamil. Extracts were vortexed
581 and centrifuged, and supernatant was transferred for LC-MS/MS analysis. LC/MS-MS was
582 performed on a Sciex Applied Biosystems Qtrap 6500+ triple-quadrupole mass spectrometer
583 coupled to a Shimadzu 30ACMP HPLC system, and chromatography was performed on an Agilent
584 Zorbax XDB-C_{18} column (3x75 mm; particle size, 3.5 µm). Milli-Q deionized water with 0.1%

585 formic acid was used for the aqueous mobile phase and 0.1% formic acid in acetonitrile for the
586 organic mobile phase. Multiple-reaction monitoring (MRM) of parent/daughter transitions in
587 electrospray positive-ionization mode was used to quantify all molecules. MRM transitions of
588 267.08/181.10 and 455.40/165.20 were used for TMZ and Verapamil respectively.

589

590 **Fluorescence microscopy and image analyses**

591 BMDMs were seeded in 8-well chamber slides (Falcon culture slide 8-well, catalog no. 08-774-
592 26), and infected with DsRed-expressing H37Rv at MOI 5. At the indicated time points, samples
593 were fixed overnight with 1% paraformaldehyde (PFA). For immunofluorescence (IF), samples
594 were permeabilized and blocked in PBS with 0.05% saponin and 3% BSA, and stained with the
595 indicated primary antibodies for 2 h at room temperature or overnight at 4°C. Primary antibodies
596 used were $p40^{phox}$ (Santa Cruz Biotechnologies), $gp91^{phox}$/NOX2 (abcam), and p62 (R&D
597 systems). Staining with alexa fluorophore-conjugated secondary antibody (Molecular Probes) was
598 done for 2 h at room temperature. Following this, the samples were washed with 0.1% Tween
599 20/PBS and mounted using Prolong Gold antifade (Thermo Fisher Scientific, catalog no. P36930).
600 Images were captured using a Nikon Eclipse Ti confocal microscope (Nikon Instruments Inc.)
601 equipped with a 60X apochromat oil-objective lens, and analyzed using NIS-Elements version
602 4.40 (Nikon). Briefly, a region of interest (ROI) was drawn around each bacterium and the mean
603 fluorescence intensity (MFI) was measured using the ROI statistics tool.

604

605 **ROS measurement assays**

606 For ROS measurement assays, the macrophages were seeded in 96 well plates (µ-Plate 96 well,
607 IBIDI catalog no. 89626). To estimate total cell ROS, the samples were treated with Cell Rox
608 green fluorescent dye (Thermo Fisher Scientific) at 5 µM for 30 minutes. The samples were
609 washed three times with PBS, and fixed overnight with 1% PFA. Mitochondrial ROS was
610 measured in live, uninfected macrophages using MitoSox fluorescent dye (Thermo Fisher
611 Scientific), at 5µM for 30 minutes. The samples were imaged using confocal microscope, and the
612 ROS signal of each cell was quantified using NIS-Elements software. Briefly, each cell was
613 converted to a ROI and the MFI was measured using the ROI statistics tool.

614

615 **Oxygen consumption rate and extracellular acidification rate**

616 BMDMs from *Cpt2* cKO mice and control littermates were plated in 96 well Seahorse plates at a
617 density of 75,000 cells per well. The cells were treated with 5nM TMZ or solvent control for 3 h.
618 After treatment, the cells were washed and placed in XF media (non-buffered RPMI 1640
619 containing 25mM glucose, 2mM L-glutamine and 1mM sodium pyruvate) with 10 % FCS. Oxygen
620 consumption rate (OCR) and extracellular acidification rates (ECAR) were measured under basal
621 conditions and following inhibitors were added: 1µM oligomycin (Sigma), 1.5µM fluorocarbonyl
622 cyanide phenylhydrazone (FCCP, Sigma), and 100 nM rotenone (Sigma) + 1µM antimycin A
623 (Sigma). Measurements were taken using a 96 well Extracellular Flux Analyzer (Seahorse
624 Bioscience, North Bellerica, MA, USA).

625

626 **Metabolomics**

627 For metabolic profiling of murine BMDMs, 15 million macrophages were seeded in 15 cm petri
628 dishes (Genesee Scientific) with 5 replicates for each condition. The next day, macrophages were
629 infected with H37Rv at an MOI 5 for 4 h as described above. The samples were washed and
630 maintained in culture medium with or without with 50 nM TMZ for 3 or 24 h. At the respective
631 time points, the samples were washed twice with sterile Hank's Balanced Salt Solution (HBSS,
632 Gibco), and the metabolites were extracted in 80% methanol (Sigma) in water (Corning). The
633 samples were stored at -80° C and shipped to Metabolon Inc., NC (www.metabolon.com) for
634 further processing and analyses.

635 At Metabolon, the samples were prepared using the automated MicroLab STAR® system from
636 Hamilton Company. After addition of recovery standards and protein removal, the extracts were
637 divided into fractions for analysis by: two separate reverse phase (RP)/ UPLC-MS/MS with
638 positive ion mode electrospray ionization (ESI), RP/UPLC-MS/MS with negative ion mode (ESI),
639 and HILIC/UPLC-MS/MS with negative ion mode ESI. All methods utilized a Waters ACQUITY
640 ultra-performance liquid chromatography (UPLC) and a Thermo Scientific Q-Exactive high
641 resolution/accurate mass spectrometer interfaced with a heated electrospray ionization (HESI-II)
642 source and Orbitrap mass analyzer operated at 35,000 mass resolution.

643

644 **Cytokine measurements**

645 Culture supernatants were harvested from uninfected or Mtb-infected BMDMs that were untreated
646 or treated with 5 or 50 nM TMZ for 24 and 72 h. The conditioned media was filter-sterilized and
647 cytokines and chemokines were measured using Milliplex MAP Mouse Cytokine/Chemokine
648 Magnetic Bead Panel (MCYTOMAG-70K, Millipore Sigma) and Procartaplex Mouse IFNα/IFNβ
649 Panel (2plex) (ThermoFisher Scientific).

650

651 **Liquid MIC determinations**

652 In 96 well plates, Mtb cultures with starting OD_{600} of 0.01, 0.05, and 0.10 were incubated with
653 increasing concentrations of drugs in triplicate. The growth of Mtb was measured at day 0, 1, 2, 3
654 and 4. The MIC was considered the minimal concentration tested that inhibited Mtb growth at 4
655 days. To assess the direct toxicity of TMZ on Mtb, H37Rv expressing the *Vibrio harvei* luciferase
656 (Rv-lux) was cultured in 7H9 broth with or without 1 mM TMZ for 7 days. Relative luminescence
657 units (RLU) were measured every 2 days at 490 nm.

658

659 **PK studies**

660 PK and plasma binding studies were performed by Alliance Pharma (PA, USA) following IV and
661 oral administration of 3 and 15 mg/kg TMZ, respectively. PK study of TMZ using Alzet osmotic
662 pumps was conducted by Paraza Pharma Inc, Canada. Briefly, Alzet osmotic pumps (model 2002,
663 Durect Corporation) were surgically implanted in C57BL/6 mice (n=5) for a subcutaneous infusion
664 at 10.66 m/k/day. Plasma TMZ concentrations were determined over the course of 48h.

665

666 **Statistics**

667 GraphPad Prism software was used to prepare plots and assess statistical significance of results
668 using unpaired Student's t-test with Welch's correction, Ordinary one-way ANOVA and Mann-
669 Whitney test.

670

671

672 **FIGURE LEGENDS**

673 **Figure 1. Inhibition of macrophage FAO restricts intracellular Mtb growth.**

674 **(A)** In the carnitine shuttle, long chain fatty acids that have been activated to acyl-CoA derivatives
675 are converted to acylcarnitines by CPT1 at the outer mitochondrial membrane. Etomoxir and
676 oxfenicine inhibit CPT1. Acylcarnitines are transported across the mitochondrial membrane by a
677 dedicated translocase. In the mitochondria, CPT2 converts acylcarnitines back to acyl-CoA and
678 carnitine. Acyl-CoA chains then undergo β-oxidation, successively generating acetyl-CoA that
679 enters the TCA cycle. Trimetazidine inhibits 3-ketoacyl-CoA thiolase, which catalyzes the release
680 of acetyl-CoA from the acyl-CoA chain. **(B-D)** Survival of Mtb (H37Rv) in BMDMs that were
681 untreated or treated for 72 h with 2 mM metformin (MET) or indicated concentrations of ETM
682 **(B),** TMZ **(C),** or OXF **(D). (E)** Survival of Mtb in BMDMs from *Cpt2* KO (*Cpt2*$^{fl/fl}$LysM-Cre^{+})
683 and littermate controls (*Cpt2*$^{fl/f}$ Cre^{-},WT) 4, 72 and 120 hpi. **(F)** Survival of Mtb in BMDMs from
684 *Cpt2* cKO and WT controls treated with ETM, TMZ, or vehicle control for 72h. CFU are expressed
685 as % of WT untreated control. **(G)** PMA-differentiated THP-1 cells were infected with Mtb and
686 treated with ETM or TMZ for 72 hpi prior to enumerating CFU. (**B-G**) Data shows mean +/- s.e.m.
687 from one representative experiment from at least 2 independent experiments.**P ≤ 0.009,
688 ***P=0.0003, ****P<0.0001, NS- not significant, one-way ANOVA (**B-D**, **F-G**) or unpaired
689 Students t-test with Welch's correction (**E**). See also **Figure S1.**

690

691 **Figure 2. FAO inhibition restricts growth of Mtb *in vivo***

692 **(A)** *Cpt2* cKO mice and littermate controls were infected by aerosol with 100-200 Mtb CFU per
693 animal, and CFU were enumerated from lungs 7 days post-infection. *P=0.04, **(B-D)** Efficacy of
694 TMZ treatment was tested in mice that were acutely infected with Mtb. Plots show total lung and

spleen CFU for the first study (B, C) and total lung CFU for the second study (D) after 2 weeks of TMZ treatment. *P=0.03, **P=0.02, ***P=0.0002. **(E)** Serum levels of TMZ were measured at the end of therapy in mice shown in (D). **(F,G)** In the chronic study, mice that were infected by aerosol with Mtb for five weeks were treated with TMZ or saline control for 2 weeks (shown in gray region) and total lung and spleen CFU were enumerated. *P=0.01, **P≤0.005, ***P=0.0002. **(H)** Serum levels of TMZ were measured in mice shown in (F) after 5 days of starting treatment (▲) and at the end of therapy (○)**.** Data shows mean +/- s.e.m., P-values calculated using Mann-Whitney rank sum test. See also **Figure S2.**

Figure 3. FAO inhibition enhances metabolic changes in response to Mtb infection.

(A) Global metabolite profiling was performed on uninfected or Mtb infected BMDMs to assess the effect of infection alone or after treatment with 50nM TMZ for 3 or 24 h. **(B)** Macrophage glycolysis was augmented in response to Mtb infection, and a sharp accumulation in glycolytic intermediates was observed. Glucose-6-phosphate was shunted to the pentose phosphate pathway for the production of PRPP and sedoheptulose-6-phosphate. The pathway heat map shows metabolite ratios in Mtb infected and uninfected (TB/Ctrl) macrophages, that were untreated (None) or TMZ treated (Drug) for 3 or 24 h. Here, significant difference (p≤0.05, three-way ANOVA) between groups are colored in green for metabolite ratio of <1 and red for ratio of >1. Light green and red colors show groups that narrowly missed statistical cutoff for significance 0.05<p<0.10. **(C)** Mtb infection induced levels of intermediates itaconate and succinate. This reflected breakpoints in the TCA cycle that are characteristic of inflammatory macrophage phenotype. Innate immune response of macrophage against the pathogen manifested as elevations in **(D)** citrulline, an iNOS by product, and **(E)** oxidized glutathione, a host redox metabolite. (C-

718 E) Graphs show ScaledImpData of different biochemicals in uninfected (UI) and infected (TB)
719 samples at the indicated time points. The line and dot show data median and mean, respectively.

720 See also **Figure S3.**

721

722 **Figure 4. FAO inhibition induces mitochondrial ROS burst required for Mtb killing.**

723 CellRox mean fluorescence intensity (MFI) of **(A)** uninfected iBMDMs that were untreated or
724 treated with 500nM TMZ for 3h, alone or in presence of mitoTEMPO (10µM) or DPI (10mM),
725 **(B)** uninfected and infected BMDMs with or without mitoTEMPO (10µM) 4hpi, (C) Mtb-infected
726 Wt and *Nox2* KO BMDMs that were untreated or treated with 5nM TMZ for 3h, and (D) Mtb-
727 infected *Cpt2* cKO and control BMDMs 24 hpi that were untreated or treated with N-acetyl
728 cysteine (NAC, 10mM). tert-Butyl hydroperoxide (tBHP, 0.25mM, 30 mins) was used as a positive
729 control. *P=0.02, **P=0.001, ****P<0.0001, NS- not significant, calculated using unpaired
730 Student's t-test with Welch's correction (A) and ordinary one-way ANOVA (B-D). (**E**) MitoSox
731 MFI of uninfected BMDMs that were untreated or treated with 500nM TMZ for 3h, alone or in
732 presence of rotenone (10µM, 30mins). *P=0.02, ****P≤0.0001, ordinary one-way ANOVA. **(F)**
733 Mtb CFU in BMDMs that were untreated or treated with 50nM TMZ alone or in combination with
734 mitoTEMPO for 120 hr. Data from one of 2 independent experiments shows mean +/-
735 s.e.m.**P=0.005 calculated using unpaired Student's t-test with Welch's correction. **(A-E)** Data
736 shown is mean +/- s.e.m. of MFI derived from individual cells in the sample. At least 100 cells
737 were analyzed from duplicate samples. For (B, E), values are expressed as %uninfected.

738 See also **Figure S4.**

739

Figure 5. FAO inhibition promotes NADPH oxidase recruitment on phagosomes.

(A) Survival of Mtb in BMDMs from *Nox2* KO and control mice that were untreated or treated with indicated concentrations of ETM and TMZ, 120 hpi.*P=0.04, ****P=0.0001, ordinary one-way ANOVA. **(B)** Immunofluorescence (IF) microscopy of gp91^{phox}/NOX2 (green) and dsRed-expressing H37Rv (red) in BMDMs that were infected and treated with 5nM TMZ or untreated for 24h. The co-localized region is shown in yellow, scale bar = 10µm. MFI of the NADPH oxidase subunits **(C)** gp91^{phox}/NOX2 and **(D)** p40^{phox} co-localized with H37Rv in BMDMs that were untreated or treated with 5nM TMZ (24hpi). **(E)** MFI of p40^{phox} co-localized with Mtb in BMDMs treated with 5nM TMZ alone or in presence of mitoTEMPO (48 hpi). (C-E) Automated image analysis was used to quantify gp91^{phox}/NOX2 or p40^{phox} MFI co-localized with over 100 bacilli in at least 2 independent experiments. Data shows mean +/- s.e.m. of MFI from around individual bacilli in the sample. *P=0.02, ****P≤0.0001 calculated using unpaired Student's t-test with Welch's correction (C-D) or ordinary one-way ANOVA (E).

Figure 6. Antimicrobial activity of FAO inhibitors depends on autophagy.

(A) Survival of Mtb was compared in FAO inhibitor treated control and *Atg5* cKO macrophages, 72hpi. **(B)** CellRox MFI in Mtb infected control and *Atg5* cKO BMDMs after TMZ treatment (5 nM, 3hr), with or without mitoTEMPO. ****P≤0.0001, unpaired Student's t-test with Welch's correction. Survival of Mtb in BMDMs from control and **(C)** *Atg14l* cKO cells 72 hpi, and **(D)** *Parkin2* KO cells 120 hpi. Data shows mean +/- s.e.m. *P=0.04, using unpaired t-test with Welch's correction in (A) or ***P=0.0002, ****P≤0.0001 using ordinary one-way ANOVA in (C, D). **(E)** IF microscopy of p62 (green) and dsRed-expressing H37Rv (red) in BMDMs treated with 5nM TMZ 24hpi. The co-localized region is shown in yellow, scale bar = 10µm. MFI of p62 co-

763 localized with Mtb was measured in BMDMs treated with 5nM TMZ alone or with mitoTEMPO
764 for **(F)** 3 or **(G)** 24 hours. **** P≤0.0001, ordinary one-way ANOVA. **(H)** IF images and **(I)** MFI
765 of p62 co-localized with Mtb in *Cpt2* KO and control BMDMs 24hpi. **(J)** MFI of p62 co-localized
766 with Δ*esxA* in BMDMs treated with TMZ for 24h. **(K)** MFI of gp91^{phox}/NOX2 co-localized with
767 Mtb in control versus *Atg5* cKO BMDMs after TMZ treatment (5nM, 24hpi). **(L)** MFI of p62 co-
768 localized with Mtb in control and Nox2KO macrophages treated with 5nM TMZ with or without
769 mitoTEMPO, 24 hpi. Data shows mean +/- s.e.m.**P=0.001, ****P≤0.0001 calculated using
770 unpaired Student's t-test with Welch's correction in (K) and ordinary one-way ANOVA for (J,L).
771 All panels show data from one representative experiment from at least 2 independent replicates.
772
773
774
775
776
777
778
779
780
781
782
783

Figure 1

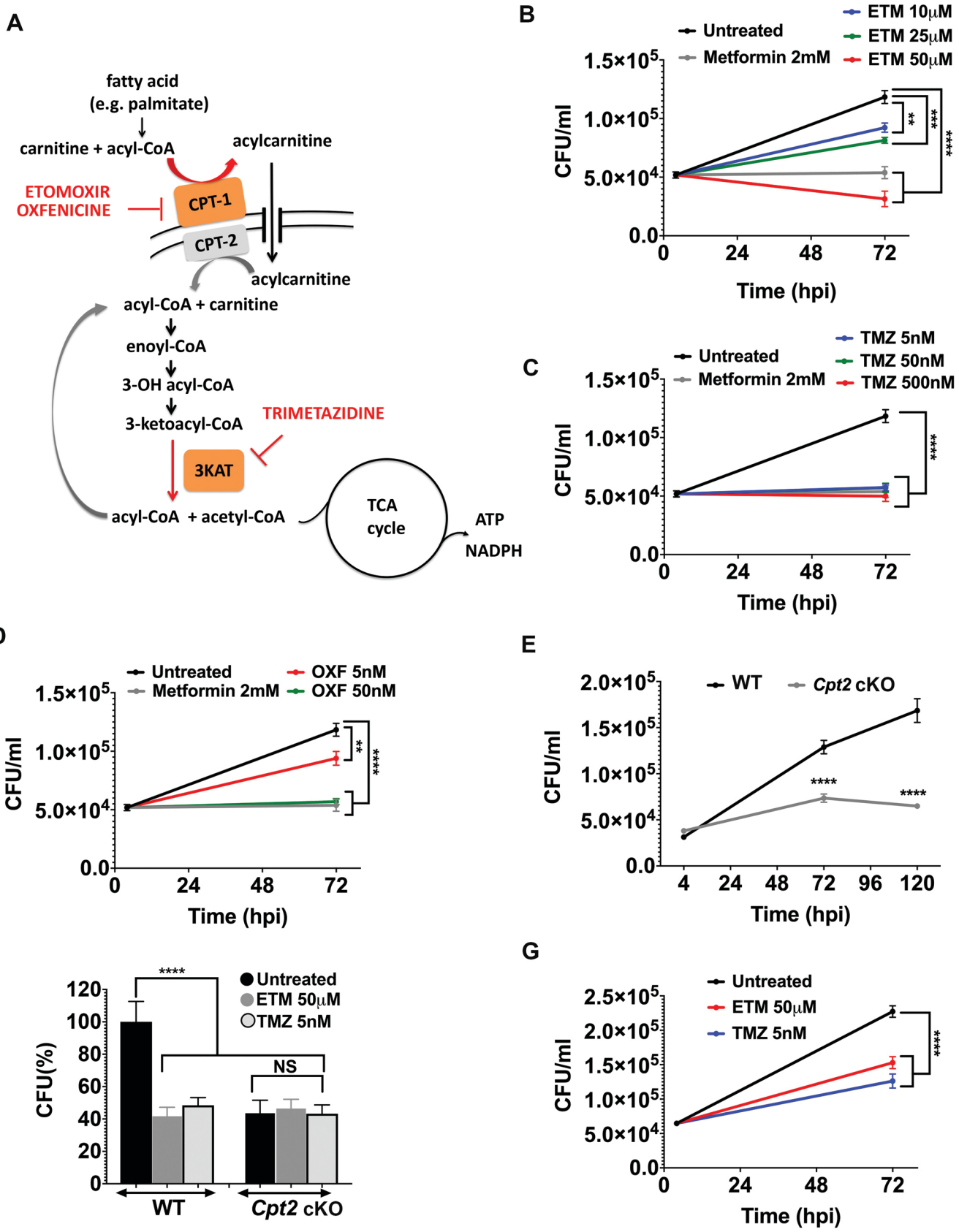

Figure 2

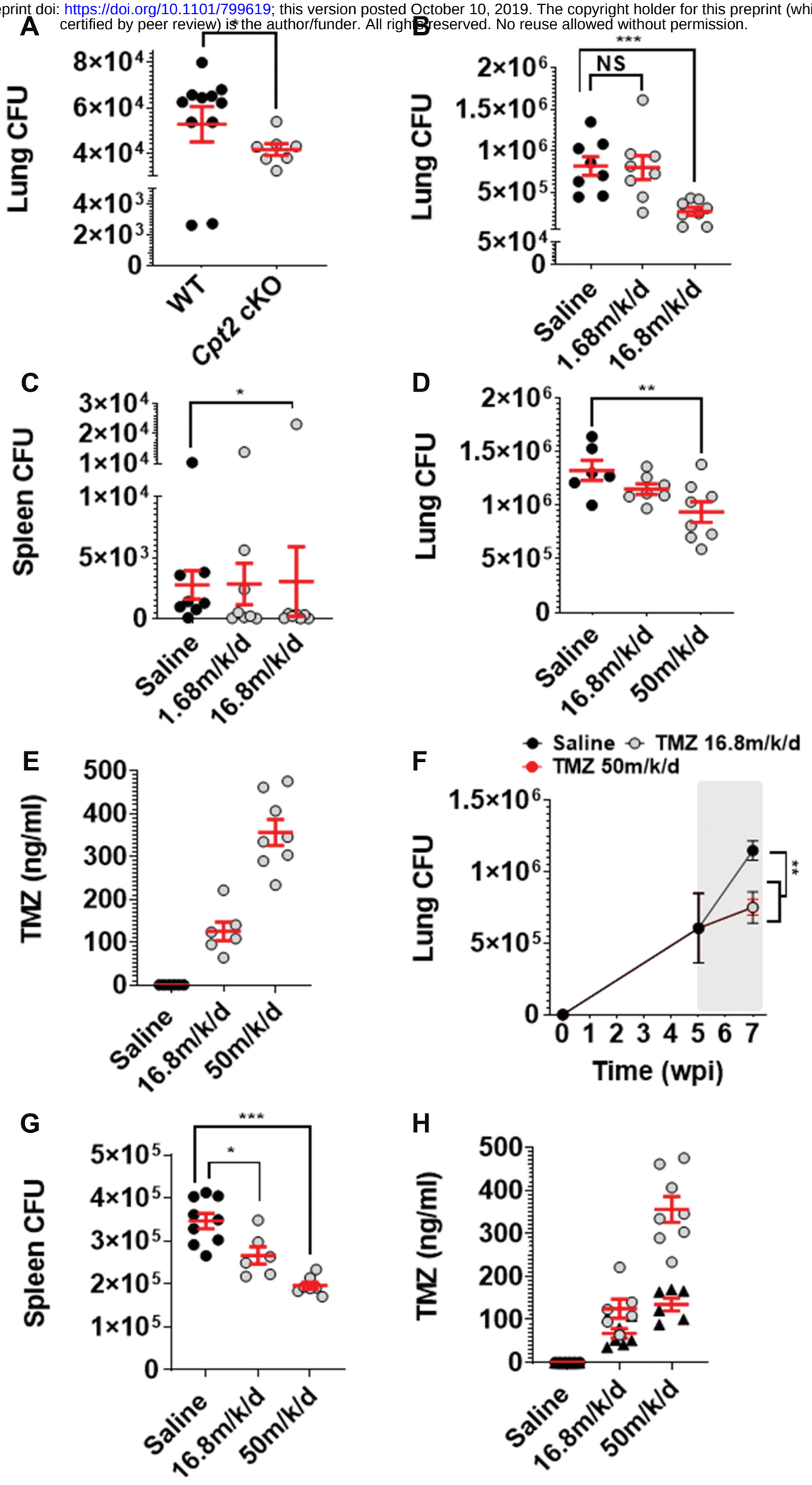

Figure 3

A

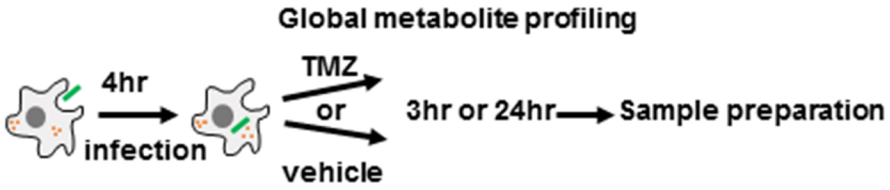

B

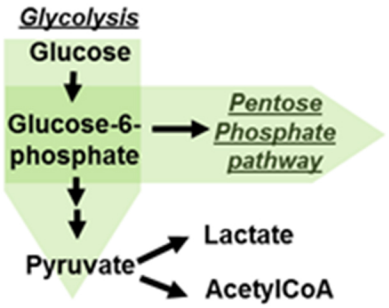

Sub Pathway	Biochemical Name	TB / Ctrl			
		None		Drug	
		3H	24H	3H	24H
Glycolysis, Gluconeogenesis, and Pyruvate Metabolism	glucose	0.83	1.02	0.83	0.92
	glucose 6-phosphate	1.55	1.12	1.50	1.52
	fructose 1,6-diphosphate/glucose 1,6-diphosphate/myo-inositol diphosphates	1.32	1.55	1.34	1.81
	3-phosphoglycerate	1.20	1.20	1.20	1.39
	phosphoenolpyruvate (PEP)	0.97	1.27	1.10	1.49
	pyruvate	0.91	1.29	1.12	1.28
	lactate	1.14	1.48	1.33	1.48
Pentose Phosphate Pathway	5-phosphoribosyl diphosphate (PRPP)	1.03	1.65	1.13	1.96
	sedoheptulose-7-phosphate	1.26	1.43	1.27	1.79

C

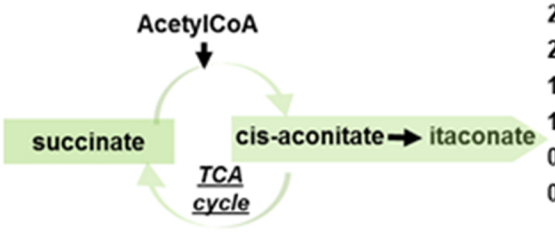

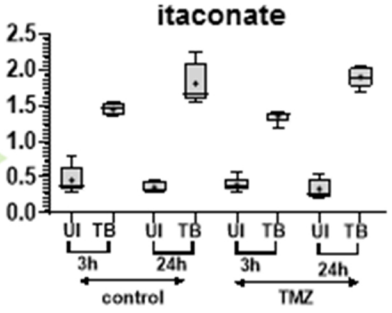

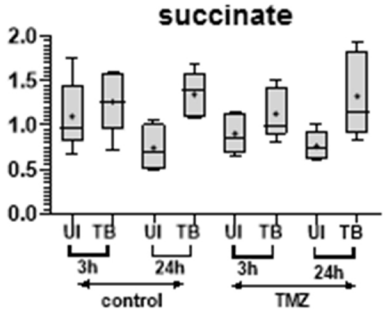

D

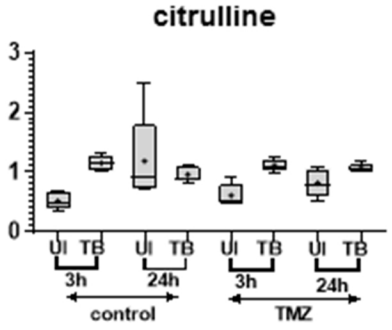

E

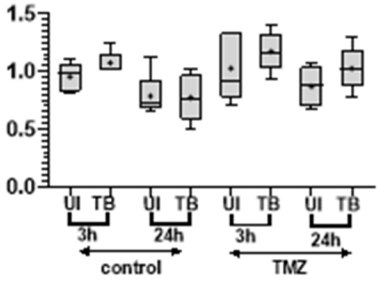

Figure 4

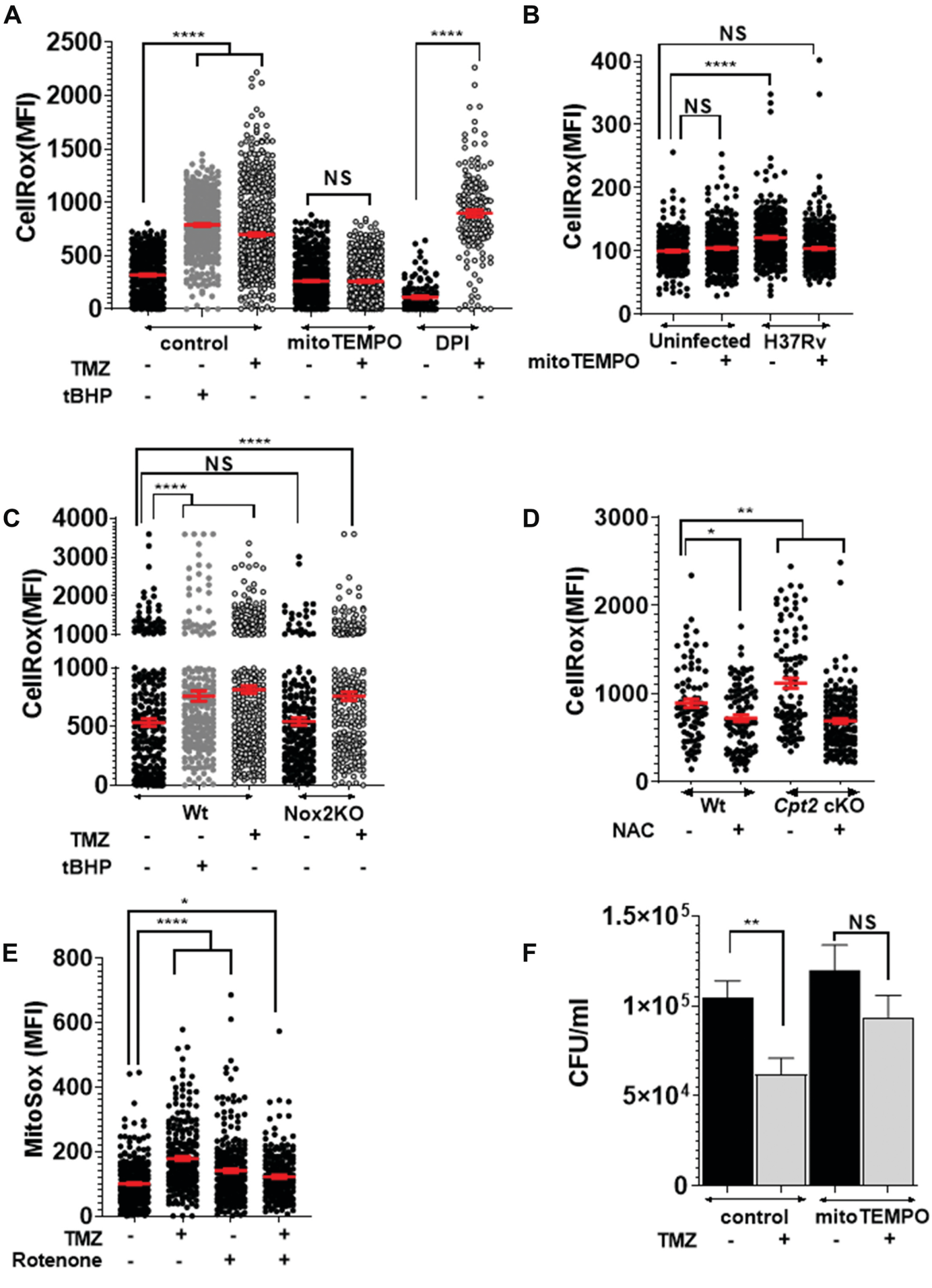

Figure 5

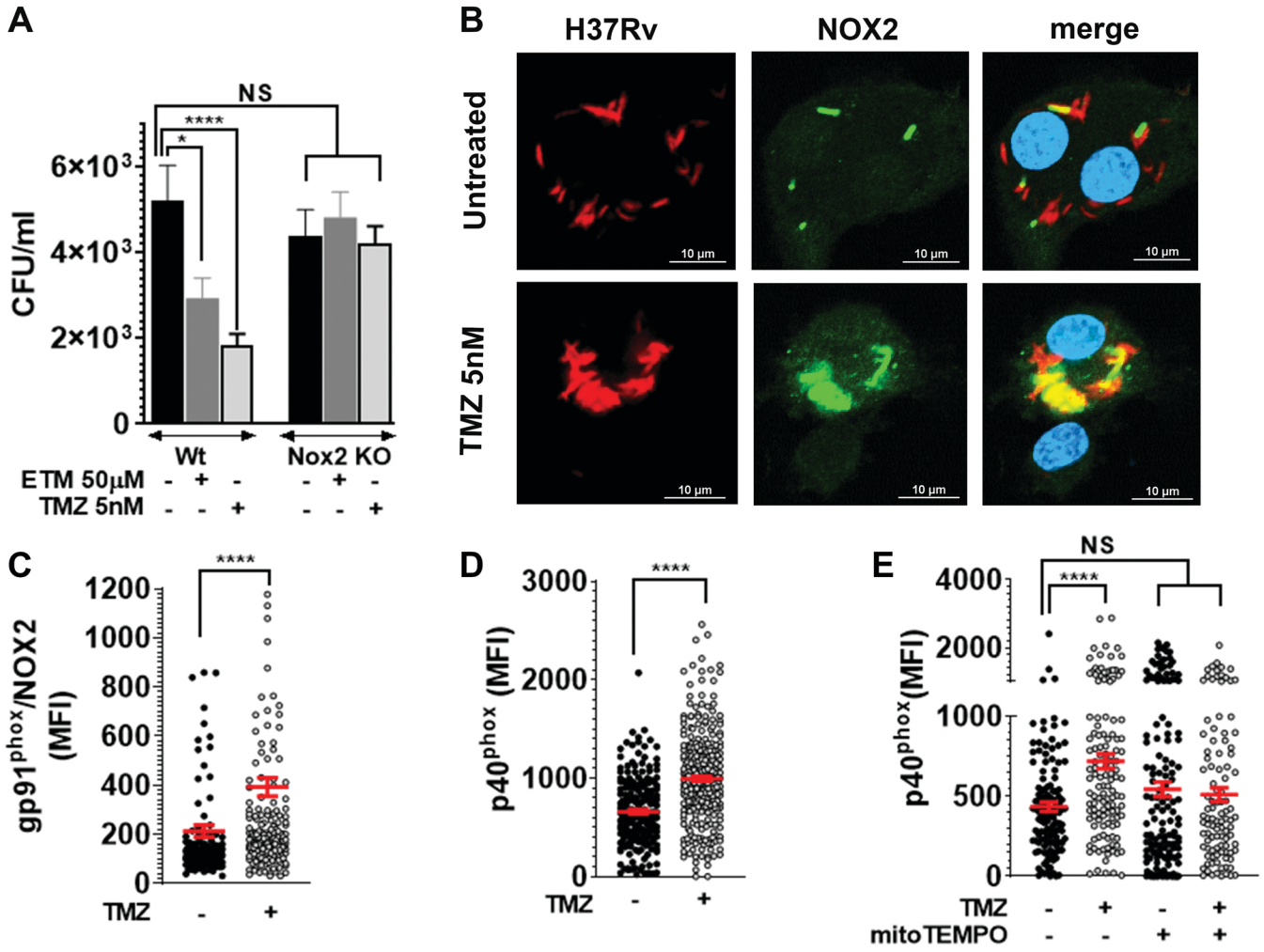
A
NS
****
*
6×10³
4×10³
2×10³
0
CFU/ml
Wt
Nox2 KO
ETM 50µM - + - - + -
TMZ 5nM - - + - - +
B
H37Rv
NOX2
merge
Untreated
TMZ 5nM
10 µm
C
****
1200
1000
800
600
400
200
0
gp91phox/NOX2 (MFI)
TMZ - +
D
****
3000
2000
1000
0
p40phox (MFI)
TMZ - +
E
NS
****
4000
2000
1000
500
0
p40phox(MFI)
TMZ - + - +
mitoTEMPO - - + +

Figure 6

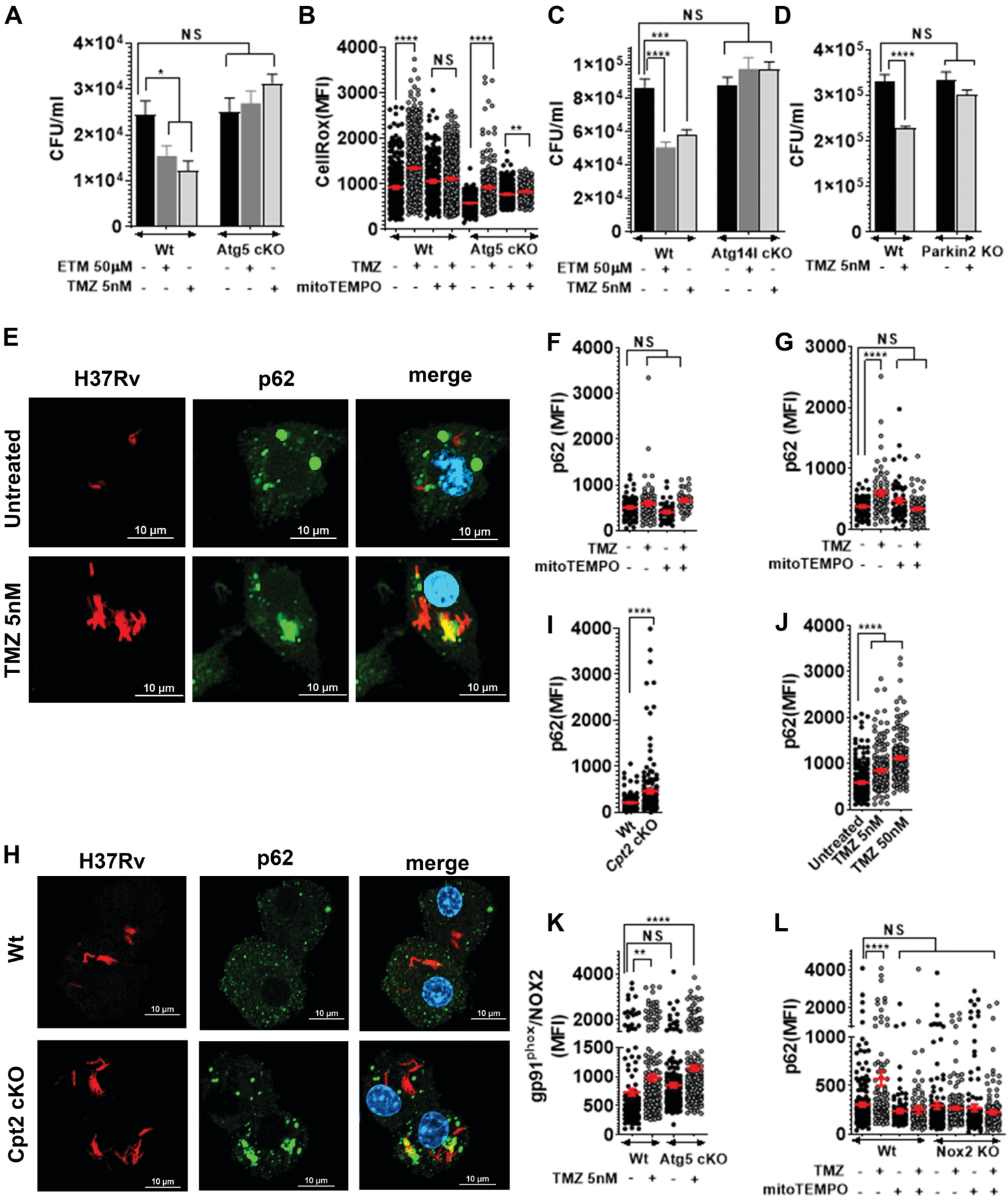

SUPPLEMENTAL INFORMATION

Figure S1. Inhibition of macrophage FAO restricts intracellular *M. tuberculosis* growth.

(A) Murine BMDMs were infected with live-dead reporter expressing H37Rv and were either untreated or treated with 50 nM TMZ for 6 days. The reporter Mtb strain constitutively expresses mCherry and has GFP controlled by a tetracycline-inducible promoter. To induce GFP expression, 200 nM anhydrotetracycline was added 2 days after infection. Metabolically active bacteria express both GFP and mCherry, whereas dead bacteria are only mCherry-positive. Representative images show more dead Mtb upon TMZ treatment as compared to control. Scale bar= 10 μm. **(B)** Macrophage were uninfected or infected with Mtb for 72h, and cell viability was assessed using calcein dye mean fluorescence intensity (MFI). Plot shows cell viability expressed as % of uninfected. Data shows mean +/- s.e.m., *P=0.03, **P≤0.0005 ordinary one-way ANOVA. (**C)** H37Rv expressing the *Vibrio harvei* luciferase (Rv-lux) was cultured in 7H9 broth with or without 1 mM TMZ for 7 days. Plot shows bacterial growth as assessed by relative luminescence units (RLU). (**D)** Minimal inhibitory concentration (MIC) of etomoxir, oxfenicine, metformin, and isoniazid (INH, positive control) was determined by culturing H37Rv for 4 days in 7H9 broth supplemented with various doses of inhibitors and measuring absorbance at 600 nm. (**E)** Intracellular growth of *M. abscessus* in BMDMs that were untreated or treated with indicated concentrations of amikacin or TMZ for 48 hours. Data shows mean +/- s.e.m., ****P≤0.0001 ordinary one-way ANOVA. (**F)** BODIPY fluorescent dye was used to stain lipid bodies in BMDMs that were infected for 24 hours with Mtb and either untreated or treated with TMZ. Shown here is mean +/- s.e.m of the % area in a cell occupied by BODIPY stain. ****P≤0.0001, unpaired Student's t-test with Welch's correction. Using extracellular flux analysis, we quantified the (**G)** oxygen consumption rate (OCR) in uninfected control and *Cpt2* cKO BMDMs treated with 5nM

807 TMZ or solvent control for 3h, followed by sequential addition of oligomycin (A), FCCP (B), and
808 rotenone plus antimycin (C). Data shows average +/- s.d. of 16 replicates.

809

810 **Figure S2. Pharmacokinetics study of TMZ in mice.**

811 The half-life of TMZ was determined in C57BL/6 mice that were administered the inhibitor **(A)**
812 orally at 15 mg/kg or **(B)** intravenously at 3 mg/kg. **(C)** TMZ (10.66 mg/kg/day) was administered
813 to female C57Bl/6 mice (n=5) for 48 hours using Alzet osmotic pumps and achieved C_{ave}- 34.5
814 ng/ml. **(D)** Protein binding of TMZ in mouse plasma (C57BL/6) was measured using rapid
815 equilibrium dialysis (n=3). Warfarin was used as a control. In humans TMZ is reportedly weakly
816 protein bound (~16%)(Harpey et al., 1988).

817

818 **Figure S3. FAO inhibition enhances metabolic changes in response to Mtb infection.**

819 Unbiased metabolite profiling was performed in BMDMs to characterize the effect of Mtb
820 infection and TMZ treatment. **(A)** Macrophage response to infection involved perturbations in
821 redox homeostasis. Increased glutathione synthesis was suggested by increased methionine to
822 cysteine conversion pathway metabolites SAM, SAH and cystathione. Ophthalmate, a
823 compositional derivative of glutathione, can reflect enhanced activity of glutathione synthetase.
824 Marked elevations were observed in gamma-glutamyl amino acids, which are formed when
825 gamma-glutamyl transpeptidase transfers the gamma-glutamyl moiety of glutathione to acceptor
826 amino acids. Infection significantly increased dihydrobiopterin and biopterin. These metabolites
827 are oxidized forms of tetrahydrobiopterin, which is a cofactor for all NOS isoforms and its
828 depletion is associated with enzyme uncoupling and ROS generation. **(B)** Increases in membrane

829 phospholipids and sphingomyelin were detected 24 hpi, which were enhanced in presence of TMZ.
830 **(C)** Tryptophan metabolism was increased with infection 24 hpi. Elevated levels of serotonin were
831 observed, with more pronounced accumulation upon TMZ treatment. Graph shows ScaledImpData
832 of serotonin in uninfected (UI) and infected (TB) samples at the indicated time points. The line
833 and dot show median and mean, respectively. Tryptophan can be converted by indoleamine 2,3-
834 dioxygenase (IDO) to kynurenine, which is further utilized for nicotinamide metabolism. TMZ
835 treatment in infected cells increased levels of metabolites in the nicotinamide pathway, suggesting
836 it might improve infection control in combination with SIRT 1 activators, as sirtuins are NAD+-
837 dependent class III histone deacetylases and activating sirtuin 1 (SIRT 1) is protective in Mtb
838 infection (Cheng et al., 2017). Other metabolic changes during infection included (**D**) increase in
839 nucleotide sugars, with a marked increase in UDP-N-acetylglucosamine/galactosamine (UDP-
840 GlcNAc) when FAO was inhibited. These metabolites are utilized in protein and lipid
841 glycosylation reactions, and UDP-GlcNAc biosynthesis was shown to be important for M2
842 macrophage polarization (Jha et al., 2015). (**E**) TMZ-induced accumulation in uracil-containing
843 pyrimidines in Mtb infected macrophages. This may indicate an increase in dihydroorotate
844 dehydrogenase (DHODH) activity, which catalyzes a rate-limiting step in the pyrimidine pathway.
845 Since DHODH can supply electrons downstream of complex I of the mitochondrial ETC, it can
846 potentially contribute to RET-ROS production. (A-F) Heatmaps show metabolite ratios in Mtb
847 infected and uninfected (TB/Ctrl) macrophages, that were untreated (None) or TMZ treated (Drug)
848 for 3 or 24 h. Here, significant difference ($p \leq 0.05$, three-way ANOVA) between groups are colored
849 in green for metabolite ratio of <1 and red for ratio of >1. Light green and red colors show groups
850 that missed the statistical cutoff for significance $0.05 < p < 0.10$.)
851

852 **Figure S4. Pro-inflammatory cytokine secretion in macrophages treated with TMZ.**

853 Supernatants from uninfected or Mtb-infected BMDMs that were untreated or treated with
854 indicated concentrations of TMZ were harvested 24 and 72 hpi. The levels of pro-inflammatory
855 cytokines and chemokines **(A)** TNF-α **(B)** IL-6, **(C)** CXCL2, **(D)** IFN-β, **(E)** CCL2, and **(F)**
856 CXCL10 were measured using a Milliplex MAP Mouse Cytokine/Chemokine Magnetic Bead
857 Panel. *P≤0.02, **P=0.004 calculated using ordinary one-way ANOVA.

858

859 **Table S1. Metabolite Differences Associated with Mtb infection and TMZ treatment**

860

861

862

863

864

865

866

867

868

869

870

871

Figure S1

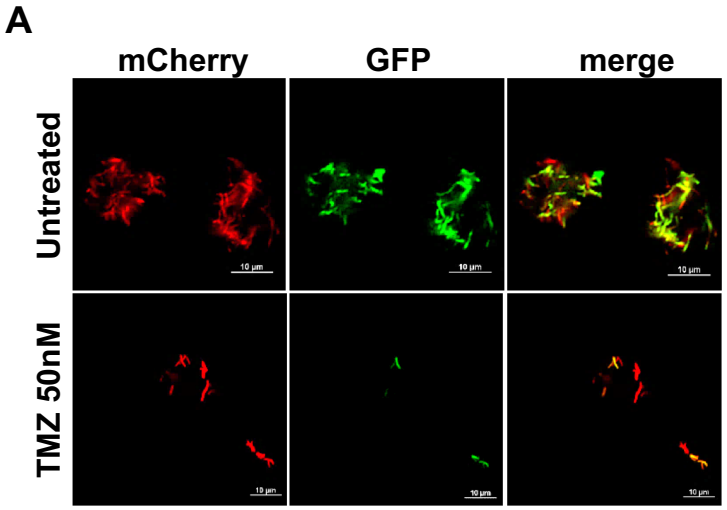

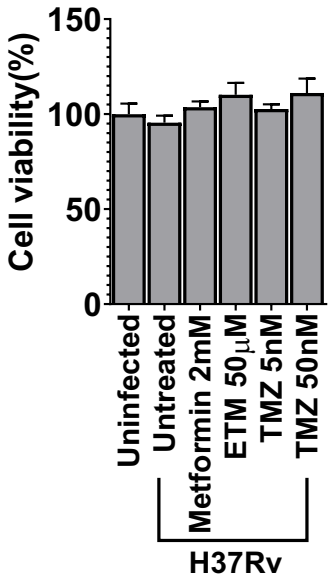

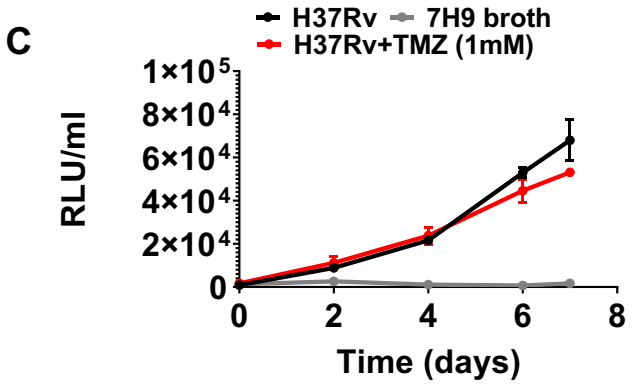

D

Antitubercular activity against H37Rv in liquid media	
Drug	**MIC**
Etomoxir	>250 μM
Oxfenicine	>140 mM
Metformin	>15 mM
INH	<0.3 μM

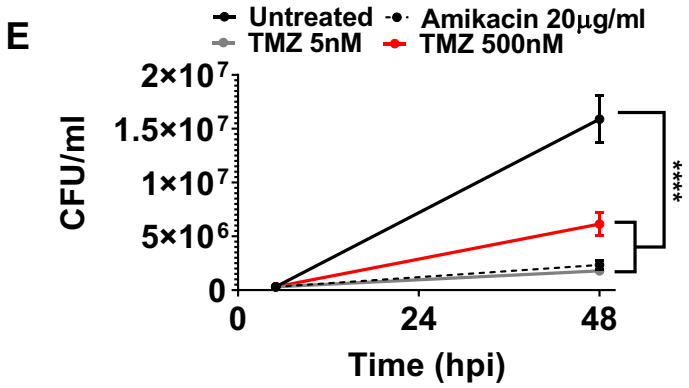

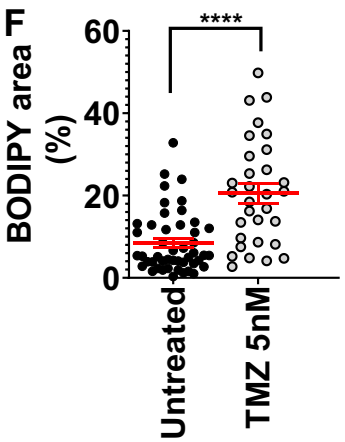

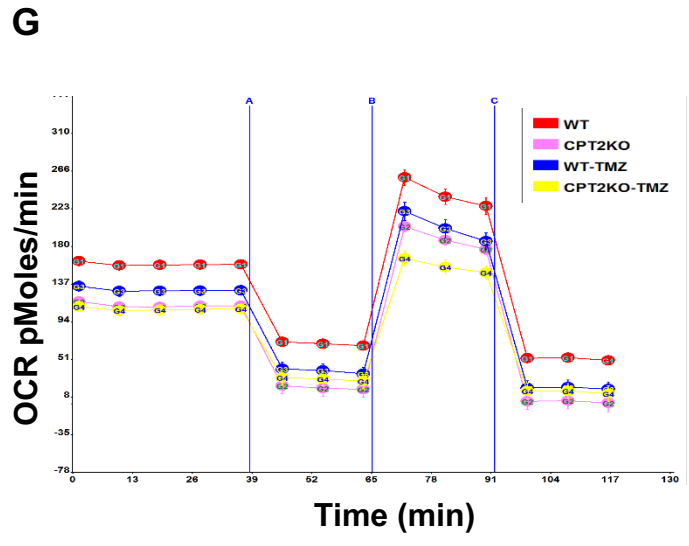

Figure S2

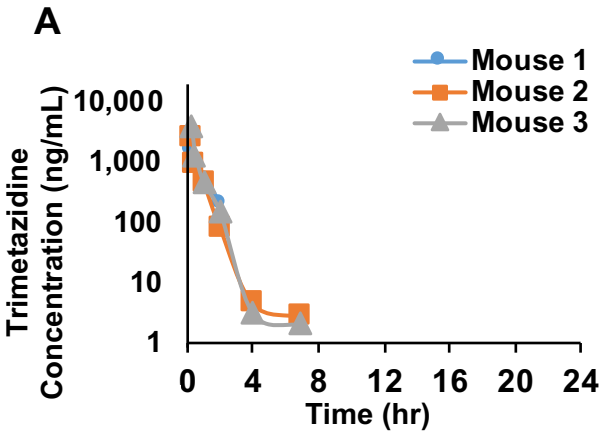

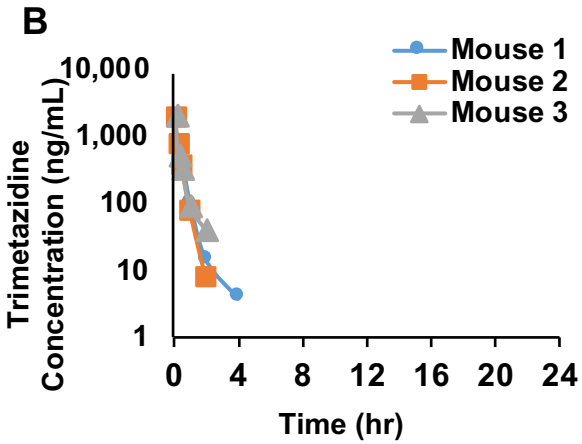

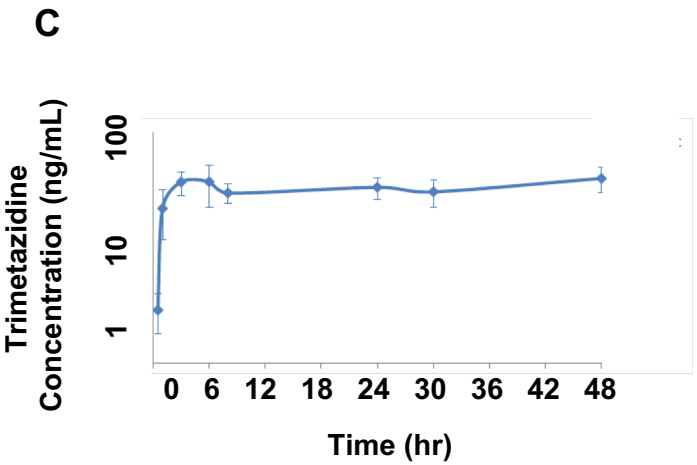

D

Protein Binding in Mouse Plasma		
Compound	Percent Free Fraction	Percent Recovery
Trimetazidine	64.86	97.94
Warfarin	4.55	110.55

Figure S3

A *Redox homeostasis*

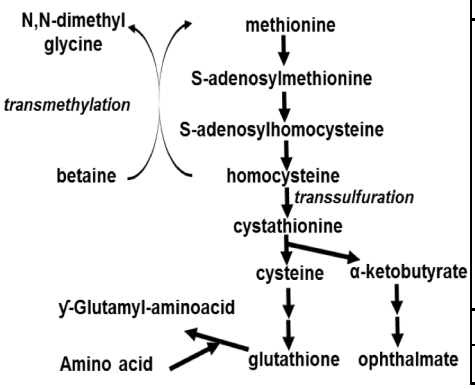

Sub Pathway	Biochemical Name	TB Ctrl None 3H	TB Ctrl None 24H	TB Ctrl Drug 3H	TB Ctrl Drug 24H
Methionine and cysteine metabolism	S-adenosylmethionine (SAM)	1.01	1.11	1.07	1.41
	S-adenosylhomocysteine (SAH)	0.90	1.30	1.02	1.48
	cystathionine	0.98	1.34	1.30	1.75
Glutathione metabolism	ophthalmate	1.68	0.98	1.49	1.23
Gamma-glutamyl amino acid	gamma-glutamylcysteine	1.41	0.98	1.39	0.97
	gamma-glutamylglutamate	1.46	1.47	1.50	1.46
	gamma-glutamylglutamine	2.19	1.93	2.14	2.16
	gamma-glutamylglycine	1.63	0.80	1.46	1.07
	gamma-glutamylisoleucine*	1.53	1.00	1.42	1.15
	gamma-glutamylleucine	1.36	0.82	1.29	1.04
	gamma-glutamyl-epsilon-lysine	1.25	0.72	1.35	0.64
	gamma-glutamylmethionine	1.71	2.28	1.45	2.40
	gamma-glutamylphenylalanine	2.73	1.84	2.36	2.34
	gamma-glutamylthreonine	1.55	0.86	1.35	0.90
	gamma-glutamylvaline	1.41	0.83	1.29	0.99
Tetrahydrobiopterin Metabolism	dihydrobiopterin	1.46	3.44	1.24	3.92
Pterin Metabolism	pterin	1.42	3.16	1.69	3.38

B *Changes in Phospholipids and sphingolipids*

Sub Pathway	Biochemical Name	TB Ctrl None 3H	TB Ctrl None 24H	TB Ctrl Drug 3H	TB Ctrl Drug 24H
Phosphatidylcholine (PC)	1-myristoyl-2-palmitoyl-GPC (14:0/16:0)	1.04	1.27	0.99	1.41
	1-myristoyl-2-arachidonoyl-GPC (14:0/20:4)*	1.15	1.11	1.12	1.32
	1-palmitoyl-2-palmitoleoyl-GPC (16:0/16:1)*	1.05	1.25	1.12	1.48
	1-palmitoyl-2-linoleoyl-GPC (16:0/18:2)	0.94	1.18	1.06	1.28
	1-palmitoyl-2-gamma-linolenoyl-GPC (16:0/18:3n6)*	1.00	1.16	1.13	1.36
	1-palmitoyl-2-dihomo-linolenoyl-GPC (16:0/20:3n3 or 6)*	0.93	1.04	1.10	1.27
	1-palmitoyl-2-docosahexaenoyl-GPC (16:0/22:6)	0.95	1.21	1.05	1.36
	1-oleoyl-2-linoleoyl-GPC (18:1/18:2)*	1.03	1.19	1.06	1.19
	1-oleoyl-2-docosahexaenoyl-GPC (18:1/22:6)*	0.91	1.13	1.04	1.34
Phosphatidylethanolamine (PE)	1,2-dipalmitoyl-GPE (16:0/16:0)*	1.35	1.25	1.27	1.39
	1-palmitoyl-2-oleoyl-GPE (16:0/18:1)	1.05	1.18	1.11	1.41
	1-palmitoyl-2-linoleoyl-GPE (16:0/18:2)	1.14	1.42	1.14	1.79
	1-palmitoyl-2-arachidonoyl-GPE (16:0/20:4)*	1.12	1.26	1.04	1.55
	1-palmitoyl-2-docosahexaenoyl-GPE (16:0/22:6)*	1.08	1.27	1.09	1.42
	1-stearoyl-2-docosahexaenoyl-GPE (18:0/22:6)*	1.22	1.07	1.14	1.23
	1-oleoyl-2-arachidonoyl-GPE (18:1/20:4)*	1.05	1.14	1.10	1.38
Phosphatidylserine (PS)	1-palmitoyl-2-oleoyl-GPS (16:0/18:1)	0.97	1.15	1.14	1.36
Phosphatidylglycerol (PG)	1-palmitoyl-2-oleoyl-GPG (16:0/18:1)	0.90	1.29	1.08	1.53
	1-oleoyl-2-linoleoyl-GPG (18:1/18:2)*	0.88	1.33	1.10	1.84
Phosphatidylinositol (PI)	1-palmitoyl-2-arachidonoyl-GPI (16:0/20:4)*	0.96	1.11	0.98	1.21
Sphingomyelins	sphingomyelin (d18:2/24:2)*	1.17	1.22	0.90	1.80
	sphingomyelin (d17:1/14:0, d16:1/15:0)*	1.31	1.22	1.22	1.63
	sphingomyelin (d18:1/14:0, d16:1/16:0)*	1.03	1.23	1.13	1.40
	sphingomyelin (d18:2/14:0, d18:1/14:1)*	1.02	1.24	1.20	1.58
	sphingomyelin (d17:1/16:0, d18:1/15:0, d16:1/17:0)*	1.01	1.17	1.07	1.28
	sphingomyelin (d17:2/16:0, d18:2/15:0)*	0.97	1.02	1.42	1.64
	sphingomyelin (d18:2/16:0, d18:1/16:1)*	1.06	1.22	1.15	1.35
Ceramide PEs	palmitoyl-sphingosine-phosphoethanolamine (d18:1/16:0)	1.02	1.16	1.06	1.28

C *Tryptophan metabolism*

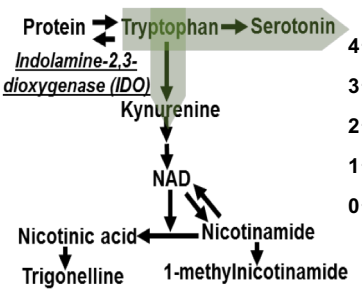

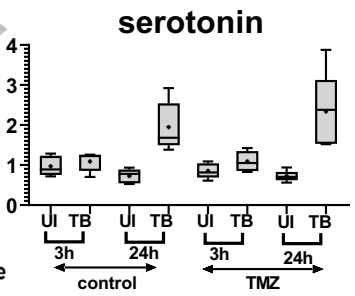

Sub Pathway	Biochemical Name	TB Ctrl None 3H	TB Ctrl None 24H	TB Ctrl Drug 3H	TB Ctrl Drug 24H
Nicotinate and Nicotinamide Metabolism	quinolinate	0.79	0.78	0.99	0.72
	nicotinamide	1.10	1.19	1.22	1.27
	nicotinamide ribonucleotide (NMN)	1.00	1.08	1.31	1.31
	nicotinamide riboside	1.02	1.11	1.19	1.24
	nicotinamide adenine dinucleotide (NAD+)	0.98	1.05	1.14	1.26
	nicotinamide adenine dinucleotide reduced (NADH)	1.01	1.17	1.04	1.37
	1-methylnicotinamide	1.35	1.11	1.14	1.25
	trigonelline (N'-methylnicotinate)	1.02	0.94	0.88	1.23
	adenosine 5'-diphosphoribose (ADP-ribose)	1.00	0.84	1.18	0.94

D *Changes in nucleotide sugars*

Sub Pathway	Biochemical Name	TB Ctrl None 3H	TB Ctrl None 24H	TB Ctrl Drug 3H	TB Ctrl Drug 24H
Nucleotide Sugar	UDP-glucose	1.33	1.57	1.44	1.75
	UDP-galactose	1.22	1.23	1.25	1.48
	UDP-glucuronate	1.34	1.47	1.38	1.66
	guanosine 5'-diphospho-fucose	1.01	1.01	1.05	1.26
	UDP-N-acetylglucosamine/galactos	1.06	0.90	1.06	1.83
	cytidine 5'-monophospho-N-acetylneuraminic acid	1.14	0.96	1.06	1.39
Mannose metabolism	mannose-6-phosphate	1.50	1.20	1.45	2.02

E

Sub Pathway	Biochemical Name	TB Ctrl None 3H	TB Ctrl None 24H	TB Ctrl Drug 3H	TB Ctrl Drug 24H
Pyrimidine Metabolism, Orotate containing	dihydroorotate	1.43	1.82	1.44	1.66
	orotate	1.47	2.26	1.67	1.43
	orotidine	1.00	1.10	1.07	1.55

Figure S4

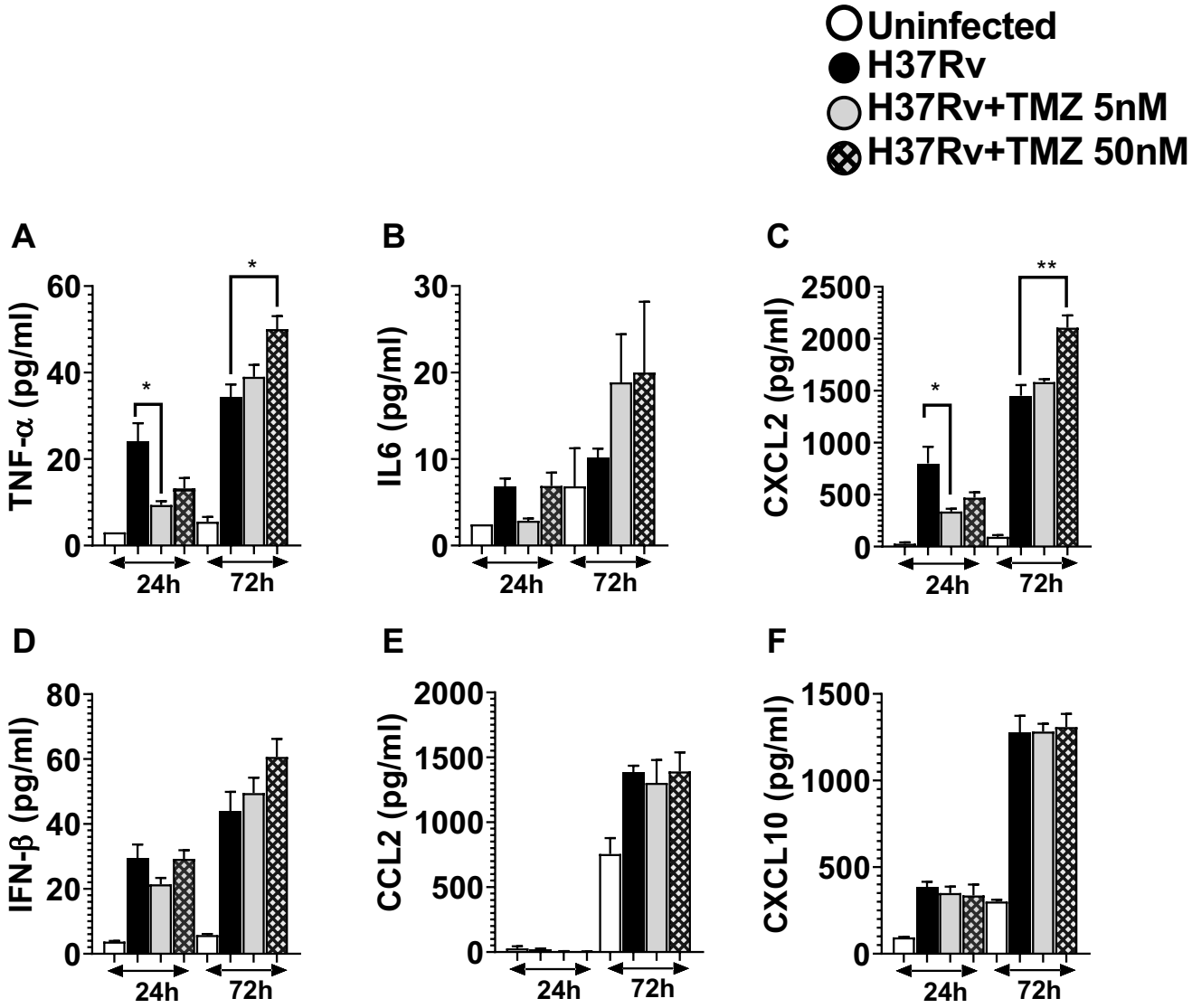

872 **REFERENCES**

873 Abuaita, B.H., Schultz, T.L., and O'Riordan, M.X. (2018). Mitochondria-Derived Vesicles
874 Deliver Antimicrobial Reactive Oxygen Species to Control Phagosome-Localized
875 Staphylococcus aureus. Cell Host Microbe *24*, 625-636.e625.

876 Almeida, P.E., Silva, A.R., Maya-Monteiro, C.M., Töröcsik, D., D'Avila, H., Dezsö, B.,
877 Magalhães, K.G., Castro-Faria-Neto, H.C., Nagy, L., and Bozza, P.T. (2009). Mycobacterium
878 bovis bacillus Calmette-Guérin infection induces TLR2-dependent peroxisome proliferator-
879 activated receptor gamma expression and activation: functions in inflammation, lipid
880 metabolism, and pathogenesis. J Immunol *183*, 1337-1345.

881 Arts, R.J.W., Carvalho, A., La Rocca, C., Palma, C., Rodrigues, F., Silvestre, R., Kleinnijenhuis,
882 J., Lachmandas, E., Gonçalves, L.G., Belinha, A.*, et al.* (2016). Immunometabolic Pathways in
883 BCG-Induced Trained Immunity. Cell Rep *17*, 2562-2571.

884 Bewley, M.A., Preston, J.A., Mohasin, M., Marriott, H.M., Budd, R.C., Swales, J., Collini, P.,
885 Greaves, D.R., Craig, R.W., Brightling, C.E.*, et al.* (2017). Impaired Mitochondrial Microbicidal
886 Responses in Chronic Obstructive Pulmonary Disease Macrophages. Am J Respir Crit Care Med
887 *196*, 845-855.

888 Brzostek, A., Pawelczyk, J., Rumijowska-Galewicz, A., Dziadek, B., and Dziadek, J. (2009).
889 Mycobacterium tuberculosis is able to accumulate and utilize cholesterol. Journal of bacteriology
890 *191*, 6584-6591.

891 Cheng, C.Y., Gutierrez, N.M., Marzuki, M.B., Lu, X., Foreman, T.W., Paleja, B., Lee, B.,
892 Balachander, A., Chen, J., Tsenova, L.*, et al.* (2017). Host sirtuin 1 regulates mycobacterial
893 immunopathogenesis and represents a therapeutic target against tuberculosis. Sci Immunol *2*.

894 Chouchani, E.T., Pell, V.R., Gaude, E., Aksentijević, D., Sundier, S.Y., Robb, E.L., Logan, A.,
895 Nadtochiy, S.M., Ord, E.N.J., Smith, A.C.*, et al.* (2014). Ischaemic accumulation of succinate
896 controls reperfusion injury through mitochondrial ROS. Nature *515*, 431-435.

897 Clausen, B.E., Burkhardt, C., Reith, W., Renkawitz, R., and Förster, I. (1999). Conditional gene
898 targeting in macrophages and granulocytes using LysMcre mice. Transgenic Res *8*, 265-277.

899 Cohen, S.B., Gern, B.H., Delahaye, J.L., Adams, K.N., Plumlee, C.R., Winkler, J.K., Sherman,
900 D.R., Gerner, M.Y., and Urdahl, K.B. (2018). Alveolar Macrophages Provide an Early
901 Mycobacterium tuberculosis Niche and Initiate Dissemination. Cell Host Microbe *24*, 439-
902 446.e434.

903 Cumming, B.M., Addicott, K.W., Adamson, J.H., and Steyn, A.J. (2018). *Mycobacterium*
904 *tuberculosis* induces decelerated bioenergetic metabolism in human macrophages. Elife *7*.

905 Daniel, J., Maamar, H., Deb, C., Sirakova, T.D., and Kolattukudy, P.E. (2011). Mycobacterium
906 tuberculosis uses host triacylglycerol to accumulate lipid droplets and acquires a dormancy-like
907 phenotype in lipid-loaded macrophages. PLoS Pathog *7*, e1002093.

908 Dézsi, C.A. (2016). Trimetazidine in Practice: Review of the Clinical and Experimental
909 Evidence. Am J Ther *23*, e871-879.

910 Divakaruni, A.S., Hsieh, W.Y., Minarrieta, L., Duong, T.N., Kim, K.K.O., Desousa, B.R.,
911 Andreyev, A.Y., Bowman, C.E., Caradonna, K., Dranka, B.P.*, et al.* (2018). Etomoxir Inhibits
912 Macrophage Polarization by Disrupting CoA Homeostasis. Cell Metab *28*, 490-503.e497.

913 Duman, C., Yaqubi, K., Hoffmann, A., Acikgöz, A.A., Korshunov, A., Bendszus, M., Herold-
914 Mende, C., Liu, H.K., and Alfonso, J. (2019). Acyl-CoA-Binding Protein Drives Glioblastoma
915 Tumorigenesis by Sustaining Fatty Acid Oxidation. Cell Metab *30*, 274-289.e275.

916 Escoll, P., and Buchrieser, C. (2019). Metabolic reprogramming: an innate cellular defence
917 mechanism against intracellular bacteria? Curr Opin Immunol *60*, 117-123.

918 Fernández-Agüera, M.C., Gao, L., González-Rodríguez, P., Pintado, C.O., Arias-Mayenco, I.,
919 García-Flores, P., García-Pergañeda, A., Pascual, A., Ortega-Sáenz, P., and López-Barneo, J.
920 (2015). Oxygen Sensing by Arterial Chemoreceptors Depends on Mitochondrial Complex I
921 Signaling. Cell Metab *22*, 825-837.

922 Galván-Peña, S., and O'Neill, L.A. (2014). Metabolic reprograming in macrophage polarization.
923 Front Immunol *5*, 420.

924 Garaude, J., Acín-Pérez, R., Martínez-Cano, S., Enamorado, M., Ugolini, M., Nistal-Villán, E.,
925 Hervás-Stubbs, S., Pelegrín, P., Sander, L.E., Enríquez, J.A.*, et al.* (2016). Mitochondrial
926 respiratory-chain adaptations in macrophages contribute to antibacterial host defense. Nat
927 Immunol *17*, 1037-1045.

928 Gleeson, L.E., Sheedy, F.J., Palsson-McDermott, E.M., Triglia, D., O'Leary, S.M., O'Sullivan,
929 M.P., O'Neill, L.A., and Keane, J. (2016). Cutting Edge: Mycobacterium tuberculosis Induces
930 Aerobic Glycolysis in Human Alveolar Macrophages That Is Required for Control of
931 Intracellular Bacillary Replication. J Immunol *196*, 2444-2449.

932 Gonzalez-Hurtado, E., Lee, J., Choi, J., Selen Alpergin, E.S., Collins, S.L., Horton, M.R., and
933 Wolfgang, M.J. (2017). Loss of macrophage fatty acid oxidation does not potentiate systemic
934 metabolic dysfunction. Am J Physiol Endocrinol Metab *312*, E381-E393.

935 Hall, C.J., Boyle, R.H., Astin, J.W., Flores, M.V., Oehlers, S.H., Sanderson, L.E., Ellett, F.,
936 Lieschke, G.J., Crosier, K.E., and Crosier, P.S. (2013). Immunoresponsive gene 1 augments
937 bactericidal activity of macrophage-lineage cells by regulating β-oxidation-dependent
938 mitochondrial ROS production. Cell Metab *18*, 265-278.

939 Harpey, C., Clauser, P., Labrid, C., Freyria, J.-L., and Poirier, J.-P. (1988). Trimetazidine, A
940 Cellular Anti-ischemic Agent. Cardiovascular Drug Reviews *6*, 292-312.

941 Huang, L., Nazarova, E.V., Tan, S., Liu, Y., and Russell, D.G. (2018). Growth of
942 *Mycobacterium tuberculosis* in vivo segregates with host macrophage metabolism and ontogeny.
943 J Exp Med *215*, 1135-1152.

Jha, A.K., Huang, S.C., Sergushichev, A., Lampropoulou, V., Ivanova, Y., Loginicheva, E., Chmielewski, K., Stewart, K.M., Ashall, J., Everts, B.*, et al.* (2015). Network integration of parallel metabolic and transcriptional data reveals metabolic modules that regulate macrophage polarization. Immunity *42*, 419-430.

Kelly, B., and O'Neill, L.A. (2015). Metabolic reprogramming in macrophages and dendritic cells in innate immunity. Cell Res *25*, 771-784.

Kim, Y.S., Lee, H.M., Kim, J.K., Yang, C.S., Kim, T.S., Jung, M., Jin, H.S., Kim, S., Jang, J., Oh, G.T.*, et al.* (2017). PPAR-α Activation Mediates Innate Host Defense through Induction of TFEB and Lipid Catabolism. J Immunol *198*, 3283-3295.

Köster, S., Upadhyay, S., Chandra, P., Papavinasasundaram, K., Yang, G., Hassan, A., Grigsby, S.J., Mittal, E., Park, H.S., Jones, V.*, et al.* (2017). Mycobacterium tuberculosis is protected from NADPH oxidase and LC3-associated phagocytosis by the LCP protein CpsA. Proc Natl Acad Sci U S A *114*, E8711-E8720.

Lachmandas, E., Beigier-Bompadre, M., Cheng, S.C., Kumar, V., van Laarhoven, A., Wang, X., Ammerdorffer, A., Boutens, L., de Jong, D., Kanneganti, T.D.*, et al.* (2016). Rewiring cellular metabolism via the AKT/mTOR pathway contributes to host defence against Mycobacterium tuberculosis in human and murine cells. Eur J Immunol *46*, 2574-2586.

Lampropoulou, V., Sergushichev, A., Bambouskova, M., Nair, S., Vincent, E.E., Loginicheva, E., Cervantes-Barragan, L., Ma, X., Huang, S.C., Griss, T.*, et al.* (2016). Itaconate Links Inhibition of Succinate Dehydrogenase with Macrophage Metabolic Remodeling and Regulation of Inflammation. Cell Metab *24*, 158-166.

Langston, P.K., Nambu, A., Jung, J., Shibata, M., Aksoylar, H.I., Lei, J., Xu, P., Doan, M.T., Jiang, H., MacArthur, M.R.*, et al.* (2019). Glycerol phosphate shuttle enzyme GPD2 regulates macrophage inflammatory responses. Nat Immunol *20*, 1186-1195.

Lee, J., Ellis, J.M., and Wolfgang, M.J. (2015). Adipose fatty acid oxidation is required for thermogenesis and potentiates oxidative stress-induced inflammation. Cell Rep *10*, 266-279.

Lionetti, V., Stanley, W.C., and Recchia, F.A. (2011). Modulating fatty acid oxidation in heart failure. Cardiovasc Res *90*, 202-209.

Manzanillo, P.S., Ayres, J.S., Watson, R.O., Collins, A.C., Souza, G., Rae, C.S., Schneider, D.S., Nakamura, K., Shiloh, M.U., and Cox, J.S. (2013). The ubiquitin ligase parkin mediates resistance to intracellular pathogens. Nature *501*, 512-516.

Manzanillo, P.S., Shiloh, M.U., Portnoy, D.A., and Cox, J.S. (2012). Mycobacterium tuberculosis activates the DNA-dependent cytosolic surveillance pathway within macrophages. Cell Host Microbe *11*, 469-480.

Marrero, J., Rhee, K.Y., Schnappinger, D., Pethe, K., and Ehrt, S. (2010). Gluconeogenic carbon flow of tricarboxylic acid cycle intermediates is critical for Mycobacterium tuberculosis to establish and maintain infection. Proc Natl Acad Sci U S A *107*, 9819-9824.

Martin, C.J., Booty, M.G., Rosebrock, T.R., Nunes-Alves, C., Desjardins, D.M., Keren, I., Fortune, S.M., Remold, H.G., and Behar, S.M. (2012). Efferocytosis is an innate antibacterial mechanism. Cell Host Microbe *12*, 289-300.

Martinez, J., Malireddi, R.K., Lu, Q., Cunha, L.D., Pelletier, S., Gingras, S., Orchard, R., Guan, J.L., Tan, H., Peng, J.*, et al.* (2015). Molecular characterization of LC3-associated phagocytosis reveals distinct roles for Rubicon, NOX2 and autophagy proteins. Nat Cell Biol *17*, 893-906.

Michelucci, A., Cordes, T., Ghelfi, J., Pailot, A., Reiling, N., Goldmann, O., Binz, T., Wegner, A., Tallam, A., Rausell, A.*, et al.* (2013). Immune-responsive gene 1 protein links metabolism to immunity by catalyzing itaconic acid production. Proc Natl Acad Sci U S A *110*, 7820-7825.

Mills, E.L., Kelly, B., Logan, A., Costa, A.S.H., Varma, M., Bryant, C.E., Tourlomousis, P., Däbritz, J.H.M., Gottlieb, E., Latorre, I.*, et al.* (2016). Succinate Dehydrogenase Supports Metabolic Repurposing of Mitochondria to Drive Inflammatory Macrophages. Cell *167*, 457-470.e413.

Munoz-Elias, E.J., and McKinney, J.D. (2005). Mycobacterium tuberculosis isocitrate lyases 1 and 2 are jointly required for in vivo growth and virulence. Nat Med *11*, 638-644.

Nair, S., Huynh, J.P., Lampropoulou, V., Loginicheva, E., Esaulova, E., Gounder, A.P., Boon, A.C.M., Schwarzkopf, E.A., Bradstreet, T.R., Edelson, B.T.*, et al.* (2018). *Irg1* expression in myeloid cells prevents immunopathology during *M. tuberculosis* infection. J Exp Med *215*, 1035-1045.

Napier, R.J., Rafi, W., Cheruvu, M., Powell, K.R., Zaunbrecher, M.A., Bornmann, W., Salgame, P., Shinnick, T.M., and Kalman, D. (2011). Imatinib-sensitive tyrosine kinases regulate mycobacterial pathogenesis and represent therapeutic targets against tuberculosis. Cell Host Microbe *10*, 475-485.

Nazarewicz, R.R., Dikalova, A.E., Bikineyeva, A., and Dikalov, S.I. (2013). Nox2 as a potential target of mitochondrial superoxide and its role in endothelial oxidative stress. Am J Physiol Heart Circ Physiol *305*, H1131-1140.

Nunes, P., Demaurex, N., and Dinauer, M.C. (2013). Regulation of the NADPH oxidase and associated ion fluxes during phagocytosis. Traffic *14*, 1118-1131.

Olive, A.J., Smith, C.M., Kiritsy, M.C., and Sassetti, C.M. (2018). The Phagocyte Oxidase Controls Tolerance to *Mycobacterium tuberculosis*. J Immunol *201*, 1705-1716.

Ouimet, M., Koster, S., Sakowski, E., Ramkhelawon, B., van Solingen, C., Oldebeken, S., Karunakaran, D., Portal-Celhay, C., Sheedy, F.J., Ray, T.D.*, et al.* (2016). Mycobacterium tuberculosis induces the miR-33 locus to reprogram autophagy and host lipid metabolism. Nat Immunol *17*, 677-686.

Pandey, A.K., and Sassetti, C.M. (2008). Mycobacterial persistence requires the utilization of host cholesterol. Proc Natl Acad Sci U S A *105*, 4376-4380.

1017 Parihar, S.P., Guler, R., Khutlang, R., Lang, D.M., Hurdayal, R., Mhlanga, M.M., Suzuki, H.,
1018 Marais, A.D., and Brombacher, F. (2014). Statin therapy reduces the mycobacterium tuberculosis
1019 burden in human macrophages and in mice by enhancing autophagy and phagosome maturation.
1020 J Infect Dis *209*, 754-763.

1021 Peyron, P., Vaubourgeix, J., Poquet, Y., Levillain, F., Botanch, C., Bardou, F., Daffe, M., Emile,
1022 J.F., Marchou, B., Cardona, P.J.*, et al.* (2008a). Foamy macrophages from tuberculous patients'
1023 granulomas constitute a nutrient-rich reservoir for M. tuberculosis persistence. PLoS Pathog *4*,
1024 e1000204.

1025 Peyron, P., Vaubourgeix, J., Poquet, Y., Levillain, F., Botanch, C., Bardou, F., Daffé, M., Emile,
1026 J.F., Marchou, B., Cardona, P.J.*, et al.* (2008b). Foamy macrophages from tuberculous patients'
1027 granulomas constitute a nutrient-rich reservoir for M. tuberculosis persistence. PLoS Pathog *4*,
1028 e1000204.

1029 Pinegin, B., Vorobjeva, N., Pashenkov, M., and Chernyak, B. (2018). The role of mitochondrial
1030 ROS in antibacterial immunity. J Cell Physiol *233*, 3745-3754.

1031 Russell, D.G., Cardona, P.J., Kim, M.J., Allain, S., and Altare, F. (2009). Foamy macrophages
1032 and the progression of the human tuberculosis granuloma. Nat Immunol *10*, 943-948.

1033 Scialò, F., Fernández-Ayala, D.J., and Sanz, A. (2017). Role of Mitochondrial Reverse Electron
1034 Transport in ROS Signaling: Potential Roles in Health and Disease. Front Physiol *8*, 428.

1035 Scialò, F., Sriram, A., Fernández-Ayala, D., Gubina, N., Lõhmus, M., Nelson, G., Logan, A.,
1036 Cooper, H.M., Navas, P., Enríquez, J.A.*, et al.* (2016). Mitochondrial ROS Produced via Reverse
1037 Electron Transport Extend Animal Lifespan. Cell Metab *23*, 725-734.

1038 Shi, L., Salamon, H., Eugenin, E.A., Pine, R., Cooper, A., and Gennaro, M.L. (2015). Infection
1039 with Mycobacterium tuberculosis induces the Warburg effect in mouse lungs. Sci Rep *5*, 18176.

1040 Singh, V., Jamwal, S., Jain, R., Verma, P., Gokhale, R., and Rao, K.V. (2012). Mycobacterium
1041 tuberculosis-driven targeted recalibration of macrophage lipid homeostasis promotes the foamy
1042 phenotype. Cell Host Microbe *12*, 669-681.

1043 Singhal, A., Jie, L., Kumar, P., Hong, G.S., Leow, M.K., Paleja, B., Tsenova, L., Kurepina, N.,
1044 Chen, J., Zolezzi, F.*, et al.* (2014). Metformin as adjunct antituberculosis therapy. Sci Transl
1045 Med *6*, 263ra159.

1046 Sun, J., Singh, V., Lau, A., Stokes, R.W., Obregón-Henao, A., Orme, I.M., Wong, D., Av-Gay,
1047 Y., and Hmama, Z. (2013). Mycobacterium tuberculosis nucleoside diphosphate kinase
1048 inactivates small GTPases leading to evasion of innate immunity. PLoS Pathog *9*, e1003499.

1049 Upadhyay, S., and Philips, J.A. (2019). LC3-associated phagocytosis: host defense and microbial
1050 response. Curr Opin Immunol *60*, 81-90.

1051 Van den Bossche, J., O'Neill, L.A., and Menon, D. (2017). Macrophage Immunometabolism:
1052 Where Are We (Going)? Trends Immunol *38*, 395-406.

1053 Vorobjeva, N., Prikhodko, A., Galkin, I., Pletjushkina, O., Zinovkin, R., Sud'ina, G., Chernyak,
1054 B., and Pinegin, B. (2017). Mitochondrial reactive oxygen species are involved in
1055 chemoattractant-induced oxidative burst and degranulation of human neutrophils in vitro. Eur J
1056 Cell Biol *96*, 254-265.

1057 Wang, T., Fahrmann, J.F., Lee, H., Li, Y.J., Tripathi, S.C., Yue, C., Zhang, C., Lifshitz, V.,
1058 Song, J., Yuan, Y.*, et al.* (2018). JAK/STAT3-Regulated Fatty Acid β-Oxidation Is Critical for
1059 Breast Cancer Stem Cell Self-Renewal and Chemoresistance. Cell Metab *27*, 1357.

1060 Wang, Y., Palmfeldt, J., Gregersen, N., Makhov, A.M., Conway, J.F., Wang, M., McCalley,
1061 S.P., Basu, S., Alharbi, H., St Croix, C.*, et al.* (2019). Mitochondrial fatty acid oxidation and the
1062 electron transport chain comprise a multifunctional mitochondrial protein complex. J Biol Chem
1063 *294*, 12380-12391.

1064 West, A.P., Brodsky, I.E., Rahner, C., Woo, D.K., Erdjument-Bromage, H., Tempst, P., Walsh,
1065 M.C., Choi, Y., Shadel, G.S., and Ghosh, S. (2011). TLR signalling augments macrophage
1066 bactericidal activity through mitochondrial ROS. Nature *472*, 476-480.

1067 Wolf, A.J., Linas, B., Trevejo-Nuñez, G.J., Kincaid, E., Tamura, T., Takatsu, K., and Ernst, J.D.
1068 (2007). Mycobacterium tuberculosis infects dendritic cells with high frequency and impairs their
1069 function in vivo. J Immunol *179*, 2509-2519.

1070 Wong, K.W., and Jacobs, W.R. (2011). Critical role for NLRP3 in necrotic death triggered by
1071 Mycobacterium tuberculosis. Cell Microbiol *13*, 1371-1384.

1072 Xue, J., Schmidt, S.V., Sander, J., Draffehn, A., Krebs, W., Quester, I., De Nardo, D., Gohel,
1073 T.D., Emde, M., Schmidleithner, L.*, et al.* (2014). Transcriptome-based network analysis reveals
1074 a spectrum model of human macrophage activation. Immunity *40*, 274-288.
1075